

Accurate Simulation of the Hubbard Model with Finite Fermionic Projected Entangled Pair States

Wen-Yuan Liu,^{1,2,*} Huanchen Zhai,¹ Ruoqing Peng,¹ Zheng-Cheng Gu,³ and Garnet Kin-Lic Chan^{1,†}

¹*Division of Chemistry and Chemical Engineering, California Institute of Technology, Pasadena, California 91125, USA*

²*Institute for Advanced Study in Physics, Zhejiang University, Hangzhou 310027, China*

³*Department of Physics, The Chinese University of Hong Kong, Shatin, New Territories, Hong Kong, China*

We demonstrate the use of finite-size fermionic projected entangled pair states, in conjunction with variational Monte Carlo, to perform accurate simulations of the ground-state of the 2D Hubbard model. Using bond dimensions of up to $D = 28$, we show that we can surpass state-of-the-art DMRG energies that use up to $m = 32000$ SU(2) multiplets on 8-leg ladders. We further apply our methodology to 10×16 , 12×16 and 16×16 lattices at 1/8 hole doping and observe the dimensional crossover between stripe orientations. Our work shows the power of finite-size fermionic tensor networks to resolve the physics of the 2D Hubbard model and related problems.

Introduction.— The two-dimensional Hubbard model is one of the most intensively studied models in condensed matter physics [1–8], and its ground state is considered central to many fundamental many-body phenomena, including quantum magnetism, Mott insulators and high-temperature superconductivity [9–13]. In the recent literature, it has also been realized in cold atom quantum simulations [14–18] and further suggested as an effective model for nickelate superconductivity [19, 20]. However, due to its intrinsic complexity, achieving accurate numerical simulations away from half-filling remains challenging.

The density matrix renormalization group (DMRG) method is recognized as a reliable method for the Hubbard model [7, 21], but accurate simulations are limited to pseudo-one-dimensional instances. Projected entangled pair states (PEPS) [22–24] are a higher-dimensional generalization of the DMRG ansatz (the matrix product state (MPS) [25]), and have evolved into an advanced numerical tool. In recent years, progress has been made with calculations using infinite-sized PEPS (iPEPS), which directly access the thermodynamic limit as a function of the unit cell in the ansatz [26–34]. Concurrently, finite-size PEPS methods, which do not assume a unit cell and complement iPEPS, have also been advanced [35–42], and have contributed to resolving the nature of the ground-state of 2D frustrated spin systems [43–47].

Despite the promise of the PEPS ansatz for fermionic lattice ground states [24, 48–51], and some studies that have employed infinite PEPS for the 2D Hubbard model [52, 53], its effectiveness for finite 2D Hubbard lattices has not yet been demonstrated, as the few works in the literature show a large gap between the accuracy of PEPS and that of DMRG on relevant lattice sizes [54]. Yet finite PEPS simulations remain desirable for several reasons. They alleviate the bias of the iPEPS unit cell, which is relevant for the long wavelength, inhomogeneous phases of the 2D Hubbard model, making finite PEPS a natural choice for studying many systems with broken translation-invariance [46], including disordered systems and optical lattice cold atoms. In challenging problems such as the 2D Hubbard model where no numerical method achieves convergence, finite PEPS also carry the advantage that they allow for a direct comparison and cross-

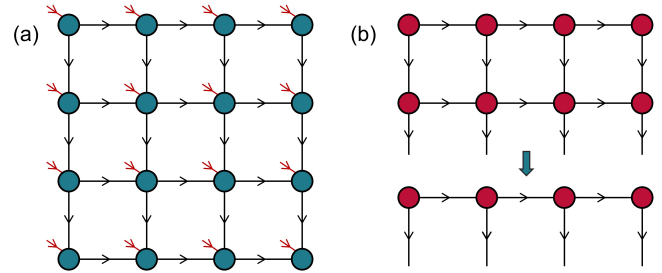


FIG. 1. (a) Graphical representation of fPEPS $|\Psi\rangle$ on a 4×4 square lattice. Red legs denote the physical degrees of freedom which are of dimension 4 for the Hubbard model, and black legs are of dimension D and control the expressive power of the fPEPS. Arrows between two connected tensors denote the relative order in the fermionic contraction. (b) For a given configuration $|\mathbf{k}\rangle$, the standard boundary-MPS method is used to compute its amplitude $\Psi(\mathbf{k})$ by contracting the corresponding single-layer tensor network.

check with methods such as DMRG and Quantum Monte Carlo which also work with finite lattices. In addition, they can be related to efforts in neural networks and machine learning, which also work in the finite setting [42, 55, 56]. The challenges for accurate finite PEPS simulation are: (i) the accessible PEPS bond dimension D , which controls the representational ability, and (ii) the optimization strategy for large lattices, given the tensors are no longer constrained by a unit cell. Finite PEPS have traditionally been studied in the context of deterministic approximate contraction algorithms, where the largest bond dimension D previously described on square lattices is $D = 8$ [54, 57]. In the 2D Hubbard model, ground state energy accuracies of (better than) 1% are required to distinguish between competing phases, and this bond dimension is insufficient.

In this work, we demonstrate a finite PEPS approach that realizes an accurate simulation of the 2D Hubbard model ground state. Specifically, using a fermionic PEPS (fPEPS) ansatz within a variational Monte Carlo algorithm, we demonstrate simulations with a bond dimension up to $D = 28$, surpassing the accuracy of the largest practical DMRG calculations on the 8-leg ladders to which DMRG is usually applied in the Hubbard model, and extending the simulations to sizes

inaccessible to DMRG, including up to 16×16 lattices, where we observe the dimensional crossover of the stripe pattern. These results thus substantially expand the capability of finite PEPS and establish it as a powerful numerical tool for the 2D Hubbard model and other challenging problems in strongly correlated electron systems.

General setup and optimization.— The Hubbard model Hamiltonian on a square lattice reads:

$$H = -t \sum_{\langle ij \rangle, \sigma} (c_{i,\sigma}^\dagger c_{j,\sigma} + h.c.) + U \sum_i n_{i\uparrow} n_{i\downarrow} - \sum_i \mu_i (n_{i\uparrow} + n_{i\downarrow}) - \sum_i h_i S_i^z, \quad (1)$$

where $\sigma = \uparrow (\downarrow)$ denotes spin up (down), $c_{i,\sigma}^\dagger$ ($c_{i,\sigma}$) is the electron creation (annihilation) operator on site i , $n_{i\uparrow}$ ($n_{i\downarrow}$) is the electron number operator for spin up (down), S_i^z is the spin- z operator, and $\langle ij \rangle$ indicates nearest neighbors. We set $t = 1$ and $U = 8$, relevant to cuprates, and consider variational states where the total electron number N_e is a good quantum number. We set the chemical potential $\mu_i = 0$ ($h_i = 0$) except in the case of charge (magnetic) pinning fields, where μ_i (h_i) is set to a non-zero value on certain sites in the initial optimization to establish a given order.

The fPEPS ansatz on the square lattice [24], is illustrated in Fig. 1(a). By defining appropriate fermionic contraction rules, fPEPS defines the wave function amplitude as a contraction of tensors associated with each lattice site similar to a conventional bosonic tensor network [22], but with additional local tensor operations that account for fermionic anti-commutation [37, 48, 58–60]. The current work uses contraction rules following the Grassmann tensor network formalism [59, 61]. To represent a wavefunction with a fixed electron number N_e , we impose U(1) charge symmetry on the local tensors [62, 63].

In conventional PEPS calculations, physical quantities are computed deterministically by contracting a double-layer tensor network comprised of the bra and ket. The computational cost scaling is $O(D^6 \chi_d^2) + O(D^4 \chi_d^3)$ on square lattices, where χ_d is an approximation bond dimension for double-layer contraction, typically chosen as $\chi_d = O(D^2)$, which leads to a scaling of $O(D^{10})$ [23, 35]. Here we employ the variational Monte Carlo (VMC) sampling technique with fPEPS, which replaces the summation over the physical degrees of freedom by an importance sampling [36, 37, 40, 64–67] of the wavefunction amplitudes $\Psi(\mathbf{k}) = \langle \mathbf{k} | \Psi \rangle$, $|\mathbf{k}\rangle = |k_1 k_2 \dots k_N\rangle$ for N sites. In this approach, only a single-layer tensor network needs to be contracted to compute $\Psi(\mathbf{k})$, which we do using the boundary-MPS contraction method [Fig. 1(b)]. The leading cost scaling of fPEPS-VMC is then $O(MD^4 \chi_s^2) + O(MD^4 \chi_s^3)$, where the latter arises from boundary-MPS contraction using SVD compression, but has a small prefactor and is not dominant in our calculations. χ_s is an approximation bond dimension for single-layer contraction, typically chosen as $\chi_s = O(D)$ (see SM [68]), which eventually leads to a scaling of $O(MD^6)$. M is the number of MC sweeps [40], typically on the order of 10000 for all sizes studied, and each sweep involves $O(N)$ samples [40]. All physical quantities

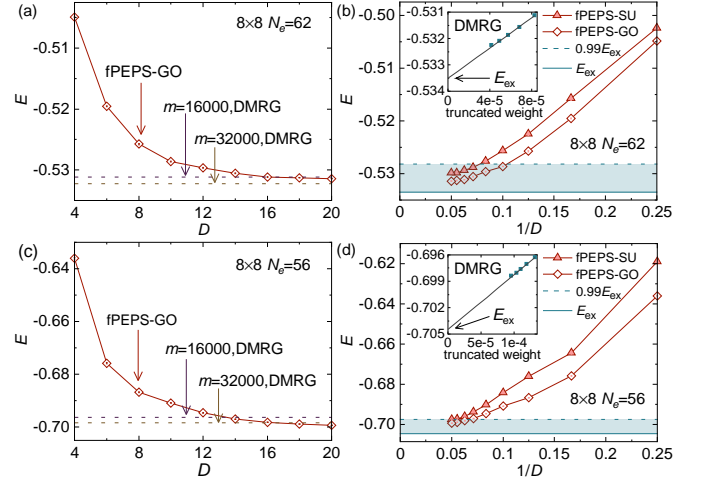


FIG. 2. The energies (per site) of the 8×8 Hubbard model at $U = 8$ with electron numbers $N_e = 62$ (a-b) and $N_e = 56$ (c-d). (a) and (c) present the energies from GO (gradient-based optimization) with respect to fPEPS bond dimension D . DMRG results with $m = 16000$ and 32000 SU(2) multiplets are shown for comparison. (b) and (d) present the $1/D$ dependence of the fPEPS energies from SU (simple update, filled triangles) and GO (unfilled diamonds). The border lines of the shaded region correspond to the extrapolated DMRG energies E_{ex} (solid) and $0.99E_{\text{ex}}$ (dashed). Insets of (b) and (d) show the extrapolation of the DMRG energies w.r.t. the truncated weights from bond dimension $m = 16000, 20000, 24000, 28000$. The energies of $m = 32000$ are also shown.

can then be evaluated by sampling, including the energy gradients with respect to the tensor elements needed for gradient optimization of fPEPS.

When optimizing the fPEPS wave function, we first use the simple update (SU) method, which has a cost scaling of $O(D^5)$ [27, 66]. During the SU optimization, we optionally add temporary pinning fields to certain sites (μ_i or h_i in Eq. 1). After converging the SU optimization, we further use gradient-based optimization (GO) methods to improve the accuracy in a subset of simulations [36, 40]. After optimization, the physical quantities are measured by MC sampling. Out of the various GO methods, we have found the stochastic reconfiguration (SR) method [69–71] to work the best (see SM [68]), thus the GO results presented are from SR optimization. Key factors enabling the accurate simulations in this work are the efficiency of SU for the orders of the 2D Hubbard model, the accessibility of large bond dimension fPEPS through MC sampling, and the use of pinning fields to establish different local orders. In the following, we will illustrate the impact of these factors.

We use open boundary conditions (OBC) along both the x and y directions, which allows for a direct comparison between fPEPS and DMRG. In the DMRG calculations U(1) \times SU(2) symmetry for the charge and spin degrees of freedom was used, and the bond dimension m in the DMRG calculations denotes the number of SU(2) multiplets.

Benchmarks on $L \times L$ systems.— We first start with bench-

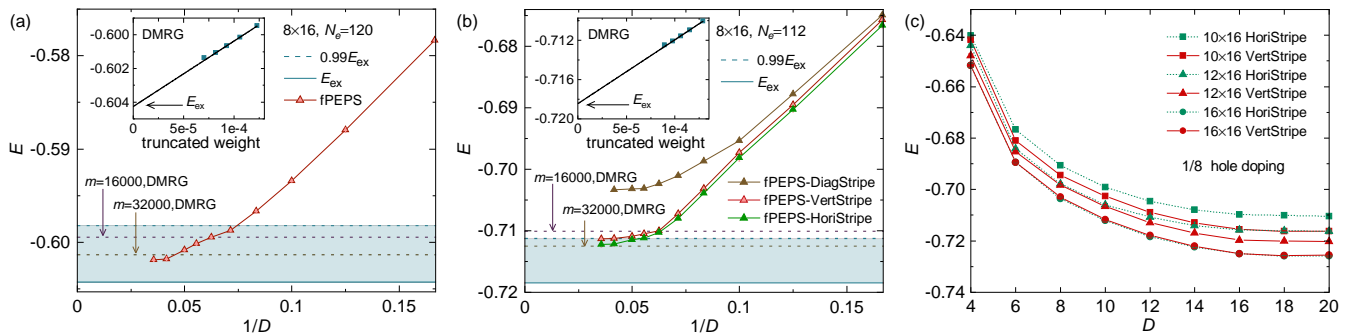


FIG. 3. Energies of the 8×16 Hubbard model at $U = 8$ with (a) $N_e = 120$ and (b) $N_e = 112$, using fPEPS with a bond dimension up to $D = 28$. In (b), fPEPS energies with diagonal (brown), vertical (violet) and horizontal (red) stripe states are shown for comparison. DMRG energies with $m = 16000$ and 32000 SU(2) multiplets are also shown. Insets of (a) and (b) show the extrapolations of DMRG energies w.r.t. the truncated weights using bond dimension $m = 16000, 20000, 24000, 28000$ (i.e. not including $m = 32000$). (c) Energies of the horizontal and vertical stripes for the $10 \times 16, 12 \times 16, 16 \times 16$ lattices at $U = 8$, with electron numbers $N_e = 140, 168, 224$, respectively, i.e., $n_h = 1/8$.

marks on small square lattices. Using converged DMRG energies as the reference, for 4×4 at half-filling $n_h = 1$ and at the hole doping concentration $n_h = 0.125$, the relative energy errors of fPEPS with $D = 16$ are 1.6×10^{-5} and 4.4×10^{-4} , respectively; for 6×6 at $n_h = 1/18$ and $n_h = 1/9$, the relative energy errors of fPEPS $D = 20$ are 1.6×10^{-3} and 4.4×10^{-3} , respectively. See SM [68]. All of these are in good agreement with the DMRG results, and could be further improved if desired, as the calculations are not expensive.

In Fig. 2, we present the fPEPS energies for the 8×8 lattice, obtained using both GO and SU optimization methods with varying D , compared to large DMRG calculations. As shown in Figs. 2(a), 2(b), for $N_e = 62$, the energy with $D = 20$ is lower than the variational DMRG result for $m = 16000$, with a relative error of 4×10^{-3} compared to the extrapolated DMRG ($m = \infty$) estimate. For $N_e = 56$ (Figs. 2(c), 2(d)) the energy with $D = 20$ using SU optimization is -0.6975 , comparable to the DMRG energy with $m = 24000$ SU(2) multiplets. With further gradient optimization, the fPEPS energy improves to $-0.69928(3)$, lower than the energy of the largest variational DMRG calculation, -0.69840 with $m = 32000$, with a relative error of 7×10^{-3} compared to the extrapolated DMRG estimate, $-0.70449(129)$. The uncertainty in the extrapolated DMRG energy is reported as one fifth of the extrapolation distance (the difference between the extrapolated and $m = 28000$ energies for the current case)[72].

In practice, we found that for the 8×8 system with $N_e = 56$, simple SU optimization often gets trapped in a local minimum characterized by a diagonal stripe, and further performing GO does not escape this local minimum. To overcome this, we used charge pinning fields with $\mu = 0.5$. For example, to stabilize a vertical stripe, we applied this field to the two middle rows of the system, starting from a random state with $D = 8$. Once the SU optimization for $D = 8$ was converged (see SM [68]), we turned off the pinning field and continued with the SU optimization, keeping the fPEPS bond dimension at $D = 24$ until convergence. Other smaller- D fPEPS states

were then obtained through a reverse process, sequentially decreasing D from 24 to smaller values, and ensuring the convergence of the SU optimization for each given D . The use of temporary pinning fields is similar to that in other DMRG optimizations [3]. In this way we were able to investigate the competition of different ordered states.

Simple update vs Gradient optimization.— Very interestingly, by comparing the energy errors of SU for a given D is only roughly twice as large as that of GO, see SM for details [68]. Meanwhile, we also observe that both SU and GO yield nearly identical patterns for the local orders for large D (see SM [68]), with only slight quantitative differences, as seen in Fig. 4(b) for the charge and spin moments in the 6×16 lattice with fPEPS $D = 20$, compared to those from DMRG. Because of this, for larger lattices we have only used SU optimization, which is much cheaper than GO, allowing for a large bond dimensions D (here, up to $D = 28$). This is advantageous in the combination with MC sampling, which enables the physical quantities of the large- D fPEPS from the SU to be efficiently evaluated.

Results on 8×16 systems.— 8-leg ladders are commonly regarded as the widest systems accessible to DMRG simulations for the 2D Hubbard model. Indeed, for the 8×16 ladder, even when using $m = 32000$ SU(2) multiplets, the DMRG calculations show large truncated weights, namely 7.0×10^{-5} and 8.9×10^{-5} respectively for $N_e = 120$ ($n_h = 1/16$) and $N_e = 112$ ($n_h = 1/8$), as illustrated in the insets of Fig. 3.

Figures 3(a) and (b) present the fPEPS energies from SU optimization up to $D = 28$. At $n_h = 1/16$, the energy decreases noticeably with increasing D until $D = 24$ and improves only slightly from $D = 24$ to 28. Note that the fPEPS $D = 16$ energy is close to the DMRG energy with $m = 16000$, and the $D = 24$ energy is $-0.60176(25)$, below the variational DMRG energy -0.60137 with $m = 32000$. The lowest fPEPS energy with $D = 28$ is $-0.60188(19)$ which is within a relative error of 4×10^{-3} of the extrapolated DMRG estimate of $-0.60426(64)$.

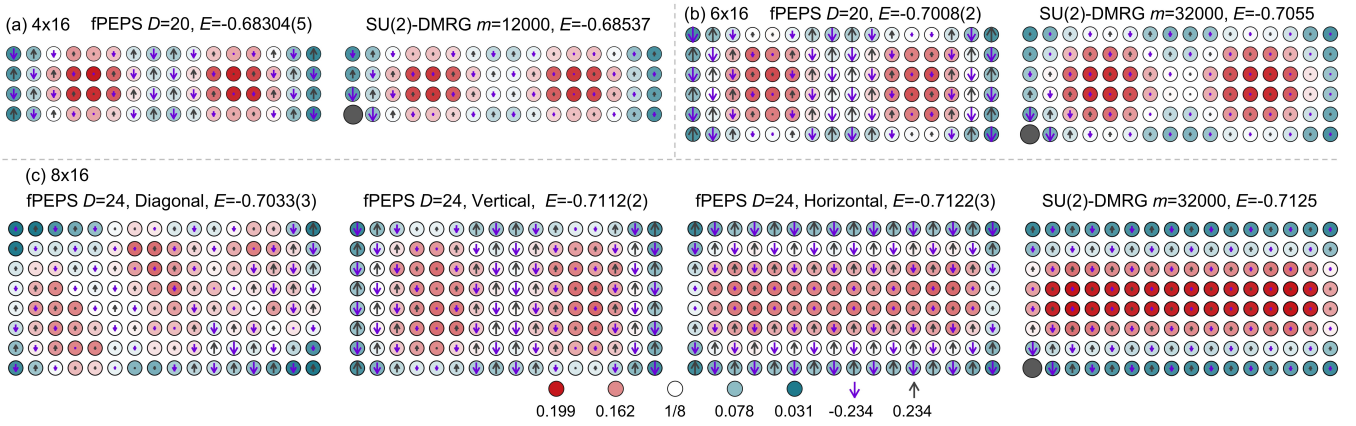


FIG. 4. Hole density and spin moment (local spin z -component for fPEPS and spin correlations for DMRG) distributions on OBC systems including (a) 4×16 , (b) 6×16 , and (c) 8×16 lattices at $U = 8$ with hole doped concentration $n_h = 1/8$, i.e. with electron number $N_e = 56, 84$ and 112 , respectively. For DMRG results, local spin z -component moments are zero due to SU(2) symmetry, and the presented arrows denote the spin correlation values $|\langle \mathbf{S}_{\text{ref}}^z \cdot \mathbf{S}_{i,j}^z \rangle|^{1/2}$ using the reference site $(0, 0)$ (filled black circles), and each arrow direction (up or down) shows the sign of $\langle \mathbf{S}_{\text{ref}}^z \cdot \mathbf{S}_{i,j}^z \rangle$. The background hole density $n_h = 1/8$ is subtracted to emphasize the fluctuation of the hole density around the background value. The magnitudes of the spin moments are represented by the sizes of the arrows. In (c) for 8×16 , three types of stripes are found in the fPEPS optimization, including the diagonal, the vertical (along y - direction) and the horizontal (along x - direction). The horizontal stripe has the lowest energy, within statistical error of the lowest DMRG energy.

At doping $n_h = 1/8$ which is of great interest [3], the DMRG $m = 32000$ calculations finds a horizontal stripe, seen in the hole density and spin correlation functions shown in Fig. 4(c). For fPEPS, we first conducted the SU optimization without pinning fields, resulting in a diagonal stripe. This diagonal stripe is at a high energy, as shown in Fig. 3(b). We then performed SU by adding temporary charge pinning fields to the central two rows to induce a similar horizontal stripe pattern to the DMRG ground-state, and the energy of this horizontal stripe with $D = 24$ is essentially the same (within statistical error) as that from DMRG using $m = 32000$. For the vertical and horizontal stripes, it is notable that the energy decreased very quickly from $D = 4$ to $D = 16$, changed slowly from $D = 16$ to $D = 24$, and showed minimal improvement from $D = 24$ to $D = 28$.

Since we found the vertical stripe phase to be the ground-state on the 4×16 and 6×16 ladders instead of the horizontal one seen above, we also imposed a temporary magnetic pinning field ($|h_i| = 0.5$) in the SU process to converge to a vertical striped state. From Fig. 3 (b) we can see that at the same D value the vertical stripe is slightly higher in energy than the horizontal stripe, indicating that the horizontal stripe indeed is favored on the 8×16 lattice. However, the energy difference between horizontal and vertical stripes is small (~ 0.001) and it is thus of interest to investigate their competition on larger lattices.

fPEPS results on larger sizes. The above detailed comparisons with DMRG explicitly demonstrate the reliability of our fPEPS results. Now we consider larger sizes including $L_y \times 16$ with $L_y = 10, 12, \text{ and } 16$, which are beyond the scope of accurate DMRG simulations. The energies of the stable horizontal and vertical stripe patterns for each fPEPS D are shown in Fig. 3(c), and the spin and hole density patterns for

$D = 20$ are presented in Fig. 5. Note that, in the case of the horizontal stripes, the pinning fields were applied to the middle two rows ($y = L_y/2$ and $L_y/2 + 1$), but SU optimization relaxed the distribution to approximately $y = L_y/4$ and $y = 3L_y/4$, resulting in the horizontal stripe pattern in Fig. 5.

In contrast to 8×16 , we find for 10×16 and 12×16 , that the vertical stripes are favoured over the horizontal ones, as seen in Fig. 3(c). For 16×16 , horizontal and vertical stripes have essentially the same energy; this is reasonable since the x - and y - directions are equivalent, and this serves as another check on the correctness of our results. The overall findings support a horizontal/vertical stripe phase with wave length $\lambda = 8$, consistent with previous studies [3], with a dimensional crossover between the two as a function of system width.

Conclusions.— In summary, we have demonstrated the power of finite-size PEPS for the 2D Hubbard model, establishing that it achieves state-of-the-art accuracy by direct comparison with DMRG energies on narrow systems, and demonstrating the ability to reach large lattice sizes, such as the 16×16 lattice. Our calculations at $1/8$ doping support the stability of the wavelength 8 stripe order seen in other studies, but allow us to further demonstrate a dimensional crossover between horizontal and vertical stripes as a function of system width. Our findings open the door towards resolving longstanding questions about fermionic ground-states via the use of finite PEPS, including questions of superconductivity in the 2D Hubbard model and related systems, while also providing a powerful classical approach for benchmarking and complementing quantum simulators.

Acknowledgment.— The DMRG calculations in this work were performed using BLOCK2[73–75], and the scripts can be found in <https://github.com/hczhai/2d-hubbard-dmrg-2024>. The computations presented in

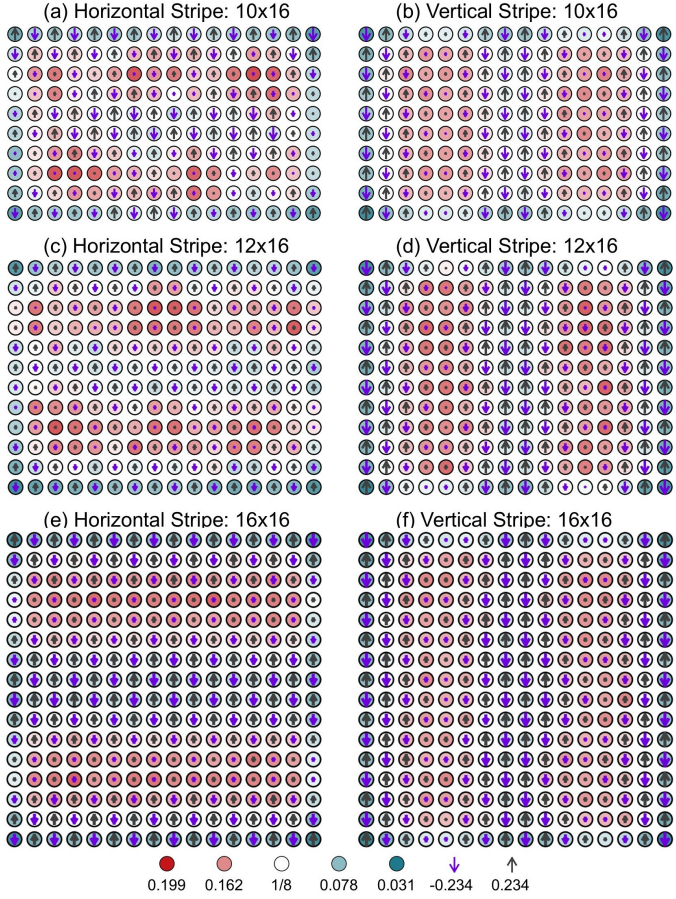


FIG. 5. Horizontal and vertical stripe patterns for different lattice sizes for $U = 8$ and hole doping $n_h = 1/8$, using fPEPS with $D = 20$. For the 10×16 and 12×16 lattices, the vertical stripe has lower energies than the horizontal ones, and for 16×16 , horizontal and vertical stripes are degenerate; see Fig. 3(c).

this work were conducted at the Resnick High Performance Computing Center, a facility supported by the Resnick Sustainability Institute at the California Institute of Technology. This work was primarily supported by the U.S. Department of Energy, Office of Science, National Quantum Information Science Research Centers, Quantum Systems Accelerator. Additional support for HZ (DMRG calculations) was provided by US Airforce Office of Scientific Research under award AFOSR-FA9550-18-1-0095. GKC is a Simons Investigator in Physics. ZCG is supported by funding from Hong Kong’s Research Grants Council (CRF C7012-21GF and RGC Research Fellow Scheme 2023/24, No. RFS2324-4S02). Wen-Yuan Liu also acknowledges additional support from a start-up grant from Zhejiang University for the final part of this work.

Supplemental Material

I. Grassmann tensor networks

There are different equivalent formalisms for fermionic tensor network computations [24, 37, 48, 58–60]. Here we use the Grassmann representation [59, 61], which is equivalent to the \mathbb{Z}_2 -graded tensor representation [76], in which all fermionic tensor operations correspond to local tensor operations. For a discussion of the relationship between this “local” formulation and a “global” ordering formulation, see Ref. [77]. For clarity and completeness, here we briefly review fermionic tensor networks in the Grassmann representation.

A. fermionic PEPS

We begin with the definition of the fermionic PEPS on a square lattice following Ref. [24]. We first consider the product state composed of a series of entangled fermion pairs on all links:

$$|\Psi_f\rangle = \prod_{\langle i,j \rangle} (1 + a_{X_i}^\dagger a_{X_j}^\dagger) |0\rangle = \prod_{\langle i,j \rangle} \mathbf{G}_{ij} |0\rangle, \quad (\text{S1})$$

where $\langle i, j \rangle$ denotes the link X (nearest neighbor) between sites i and j , and $a_{X_i}^\dagger$ and $a_{X_j}^\dagger$ are fermionic creation operators on sites i and j at the ends of the link X . We call the fermions created by $a_{X_i}^\dagger$ and $a_{X_j}^\dagger$, virtual fermions, by convention.

Now we map the virtual fermionic space on site i to the physical fermionic space via the projector:

$$\mathbf{P}_i = \sum_{m_i} \sum_{lurd=0}^1 T_{lurd}^{[m_i]} c^{\dagger m_i} a_{L_i}^l a_{U_i}^u a_{R_i}^r a_{D_i}^d, \quad (\text{S2})$$

where c^\dagger is the physical fermionic creation operator at site i , and a_{X_i} ($X = L, U, R, D$) is the fermionic annihilation operator on site i connecting its neighbouring sites in the left, up, right or down directions. For simplicity, we consider the physical and virtual fermionic degrees of freedom to both be of dimension 2, i.e., m and x ($x = l, u, r, d$) are 0 or 1. To ensure that the parity of the PEPS is well defined, we can assume all elements $T_{lurd}^{[m_i]}$ are zero if $(l + u + r + d + m_i)$ is odd. Then, the fermionic PEPS is expressed as:

$$|\Psi\rangle = \left\langle \prod_i \mathbf{P}_i \prod_{\langle i,j \rangle} \mathbf{G}_{ij} \right\rangle_0 |0\rangle \quad (\text{S3})$$

Here $\langle \dots \rangle_0$ denotes the expectation of the virtual fermions over the vacuum (i.e. integrating out the virtual fermionic degrees of freedom). The fPEPS bond dimension here corresponds to $D = 2$.

For general fPEPS with a bond dimension D , by introducing multiple fermionic modes, we can write down the formal

generalization as:

$$|\Psi_f\rangle = \prod_{(i,j)} \left(\sum_{n=0}^{D-1} a_{X_{i,n}}^{\dagger p(n)} a_{X_{j,n}}^{\dagger p(n)} \right) |0\rangle = \prod_{(i,j)} \mathbf{G}_{ij} |0\rangle, \quad (\text{S4})$$

$$\mathbf{P}_i = \sum_{m_i} \sum_{lurd=0}^{D-1} T_{lurd}^{[m_i]} c^{\dagger m_i} a_{L_{i,l}}^{p(l)} a_{U_{i,u}}^{p(u)} a_{R_{i,r}}^{p(r)} a_{D_{i,d}}^{p(d)}, \quad (\text{S5})$$

Here $a_{X_{i,n}}^{\dagger}$ is the fermionic operator to create a fermionic mode, and $p(n)$ is either 0 or 1 following the parity of this fermionic mode.

Specifically, imagine there are z fermions with 2^z associated fermion modes, and $a_{X_{i,n}}^{\dagger} |0\rangle = |n_1 n_2 \cdots n_z\rangle$ ($n_k = 0$ or 1) with a parity $p(n) = \text{mod}(\sum_{k=1}^z n_k, 2)$. The bond dimension D represents the D fermionic modes corresponding to the 2^z different occupancies, and the subscript n in $a_{X_{i,n}}^{\dagger}$ distinguishes the different modes. Since only the even or odd parity matters for the fermionic signs, $a_{X_{i,n}}^{\dagger}$ works basically as a conventional fermionic operator, and the fPEPS still has the form Eq. (S3). As mentioned above $|\Psi\rangle$ is required to have a well defined parity, say even parity, thus we assume all elements $T_{lurd}^{[m_i]}$ are zero if $[p(m_i) + p(l) + p(u) + p(r) + p(d)]$ is odd.

When contracting fermionic tensor networks, we need to be careful with the order of the fermionic operators, and any change in order requires following the anticommutation relations. Below we adopt the Grassmann formalism in which the possible signs caused by anticommutators can be computed locally [59, 61].

B. Grassmann Tensor Representations

1. Grassmann algebra

In the standard Grassmann algebra, for the Grassman variable η_i and its conjugate $\bar{\eta}_i$, we have

$$\eta_i \eta_j = -\eta_j \eta_i, \quad \bar{\eta}_i \bar{\eta}_j = -\bar{\eta}_j \bar{\eta}_i, \quad \eta_i \bar{\eta}_j = -\bar{\eta}_j \eta_i, \quad (\text{S6})$$

$$\int d\eta_i \eta_j = \int d\bar{\eta}_i \bar{\eta}_j = \delta_{ij}. \quad (\text{S7})$$

Considering two Grassmann functions $\mathbf{A}(\xi, \bar{\eta}) = A_{00} + A_{10}\xi + A_{01}\bar{\eta} + A_{11}\xi\bar{\eta}$ and $\mathbf{B}(\eta, \beta) = B_{00} + B_{10}\eta + B_{01}\beta + B_{11}\eta\beta$, the scalar product obtained by integrating out the variable η and its conjugate $\bar{\eta}$ is defined with a Grassmann metric $e^{-\bar{\eta}\eta}$ [78],

$$\begin{aligned} \int_{\eta} \mathbf{A}(\xi, \bar{\eta}) \mathbf{B}(\eta, \beta) &= \int d\eta d\bar{\eta} e^{-\bar{\eta}\eta} \mathbf{A}(\xi, \bar{\eta}) \mathbf{B}(\eta, \beta) \\ &= \int d\eta d\bar{\eta} (1 - \eta\bar{\eta}) (A_{00} + A_{10}\xi + A_{01}\bar{\eta} + A_{11}\xi\bar{\eta}) \\ &\quad \times (B_{00} + B_{10}\eta + B_{01}\beta + B_{11}\eta\beta) \\ &= A_{00}B_{00} + A_{01}B_{10} + (A_{10}B_{00} + A_{11}B_{10})\xi \\ &\quad + (A_{00}B_{01} + A_{01}B_{11})\beta + (A_{10}B_{01} + A_{11}B_{11})\xi\beta \end{aligned} \quad (\text{S8})$$

In the above calculation, the existence of the symbol $d\eta d\bar{\eta}$ and the metric $e^{-\bar{\eta}\eta}$, makes the Grassmann integral

computations in Eq. (S8) somewhat tedious. We find the action of “ $\int d\eta d\bar{\eta} e^{-\bar{\eta}\eta}$ ” can be conveniently realized using a simple rule defined as

$$\int \bar{\eta}_i^{p(i)} \eta_j^{p(j)} = \delta_{ij} \delta_{p(i), p(j)}, \quad \int \eta_j^{p(j)} \bar{\eta}_i^{p(i)} = (-1)^{p(i)} \delta_{ij} \delta_{p(i), p(j)}. \quad (\text{S9})$$

The subscript i in $\bar{\eta}_i$ specifies the species of Grassmann variable, and $p(i) = 0$ or 1 is its parity, denoting the absence or presence of the variable.

With this, we reconsider Eq. (S8). We first write the Grassmann functions $\mathbf{A}(\xi, \bar{\eta})$ and $\mathbf{B}(\eta, \beta)$ in a Grassmann tensor form, i.e., $\mathbf{A}(\xi, \bar{\eta}) = \sum_{l_1 l_2} A_{l_1 l_2} \xi^{p(l_1)} \bar{\eta}^{p(l_2)}$ and $\mathbf{B}(\eta, \beta) = \sum_{l_3 l_4} B_{l_3 l_4} \eta^{p(l_3)} \beta^{p(l_4)}$, where $p(l_i)$ is 0 (1) when the Grassmann variable is absent (present). Using Eq. (S9), then the integral over η and its conjugate $\bar{\eta}$ can be directly read out

$$\begin{aligned} &\int_{\eta} \mathbf{A}(\xi, \bar{\eta}) \mathbf{B}(\eta, \beta) \\ &= \int \sum_{l_1 l_2 l_3 l_4} (A_{l_1 l_2} \xi^{p(l_1)} \bar{\eta}^{p(l_2)}) (B_{l_3 l_4} \eta^{p(l_3)} \beta^{p(l_4)}) \\ &= \sum_{l_1 l_2 l_3 l_4} A_{l_1 l_2} B_{l_3 l_4} \xi^{p(l_1)} \left(\int \bar{\eta}^{p(l_2)} \eta^{p(l_3)} \right) \beta^{p(l_4)} \\ &= \sum_{l_1 l_2 l_3 l_4} A_{l_1 l_2} B_{l_3 l_4} \xi^{p(l_1)} \delta_{l_2 l_3} \beta^{p(l_4)} \\ &= \sum_{l_1 l_2 l_4} A_{l_1 l_2} B_{l_2 l_4} \xi^{p(l_1)} \beta^{p(l_4)}, \end{aligned} \quad (\text{S10})$$

which is identical to Eq. (S8), showing the validity of Eq. (S9).

Therefore, with the help of Eq. (S9), we can replace the Grassmann algebra of Eqs. (S6-S7) by the following relations, which are simpler for our fermionic computations:

$$\eta_i \eta_j = -\eta_j \eta_i, \quad \bar{\eta}_i \bar{\eta}_j = -\bar{\eta}_j \bar{\eta}_i, \quad \eta_i \bar{\eta}_j = -\bar{\eta}_j \eta_i, \quad (\text{S11})$$

$$\int \bar{\eta}_i^{p(i)} \eta_j^{p(j)} = \delta_{ij} \delta_{p(i), p(j)}, \quad \int \eta_j^{p(j)} \bar{\eta}_i^{p(i)} = (-1)^{p(i)} \delta_{ij} \delta_{p(i), p(j)}. \quad (\text{S12})$$

Here $p(i)$ is either 0 or 1, denoting the absence or presence of the Grassmann variable. Intuitively, the Grassmann relations realize the action of the fermionic operators a_i^{\dagger} and a_i through the Grassmann variables η_i and its conjugate $\bar{\eta}_i$. The integral in Eq. (S12) is similar to the expectation value of $a_i a_j^{\dagger}$ over the vacuum, and mimics the sum over virtual fermionic degrees of freedom in fermionic tensor networks. Using the basic relations Eqs. (S11-S12), the following rules can be derived directly.

2. Grassmann tensor operations

A general rank- r Grassmann tensor containing m η -type variables and $(r - m)$ $\bar{\eta}$ -type variables can be expressed as:

$$\mathbf{T} = \sum_{l_1 l_2 \dots l_r} T_{l_1 l_2 \dots l_r} \eta_{X_1, l_1}^{p(l_1)} \cdots \eta_{X_m, l_m}^{p(l_m)} \bar{\eta}_{X_{m+1}, l_{m+1}}^{p(l_{m+1})} \cdots \bar{\eta}_{X_r, l_r}^{p(l_r)}. \quad (\text{S13})$$

X_i labels the Grassmann numbers on different tensor legs, and on a given leg X_i , l_i is used to distinguish different Grassmann variables on this leg, and $p(l_i)$ is the corresponding parity, either 0 or 1. $T_{l_1 l_2 \dots l_r}$ is a number, i.e. the tensor element. When working with the Grassmann tensor \mathbf{T} , we not only need to deal with the elements $T_{l_1 l_2 \dots l_r}$, but also consider the order of the Grassmann variables. In the following we will omit the label of leg X_i in the expression of \mathbf{T} for convenience:

$$\mathbf{T} = \sum_{l_1 l_2 \dots l_r} T_{l_1 l_2 \dots l_r} \eta_{l_1}^{p(l_1)} \dots \eta_{l_m}^{p(l_m)} \bar{\eta}_{l_{m+1}}^{p(l_{m+1})} \dots \bar{\eta}_{l_r}^{p(l_r)}. \quad (\text{S14})$$

Tensor parity. Generally, we can choose Grassmann tensors to have a definitive parity $p(\mathbf{T})$, that is all tensor elements $T_{l_1 l_2 \dots l_r}$ satisfy:

$$T_{l_1 l_2 \dots l_r} = 0, \quad \text{if} \quad \text{mod}(p(l_1) + p(l_2) + \dots + p(l_r), 2) = 1 - p(\mathbf{T}).$$

If $p(\mathbf{T}) = 0$ (1), we say the tensor has an even (odd) parity.

Note for the odd-parity tensor \mathbf{T} with $p(\mathbf{T}) = 1$, it can always be converted into an even-parity tensor $\tilde{\mathbf{T}}$ with $p(\tilde{\mathbf{T}}) = 0$ by introducing an extra tensor leg. Specifically, for an odd-parity tensor \mathbf{T} ,

$$T_{l_1 l_2 \dots l_r} = 0, \quad \text{if} \quad \text{mod}(p(l_1) + p(l_2) + \dots + p(l_r), 2) = 0.$$

After adding an extra tensor leg k ,

$$\tilde{T}_{l_1 l_2 \dots l_r k} = 0, \quad \text{if} \quad \text{mod}(p(l_1) + p(l_2) + \dots + p(l_r) + k, 2) = 1,$$

where the leg k is dimension-1 with an odd parity. Then the tensor $\tilde{\mathbf{T}}$ comprised of $\tilde{T}_{l_1 l_2 \dots l_r k}$ has an even parity. Such a parity changing operation is very convenient for practical fermionic tensor network computations [48].

Permutation. For a Grassmann tensor, if we exchange the positions of any two Grassmann variables η_{l_i} and $\eta_{l_{i+1}}$, the resulting Grassmann tensor is

$$\begin{aligned} \mathbf{T}' &= \sum_{l_1 \dots l_r} T_{l_1 \dots l_r} \eta_{l_1}^{p(l_1)} \dots \eta_{l_i}^{p(l_i)} \eta_{l_{i+1}}^{p(l_{i+1})} \dots \bar{\eta}_{l_r}^{p(l_r)} \\ &= \sum_{l_1 \dots l_r} (-1)^{[p(l_i) * p(l_{i+1})]} T_{l_1 \dots l_r} \eta_{l_1}^{p(l_1)} \dots \eta_{l_{i+1}}^{p(l_{i+1})} \eta_{l_i}^{p(l_i)} \dots \bar{\eta}_{l_r}^{p(l_r)}. \end{aligned} \quad (\text{S15})$$

This is basically the result of the anti-commutation relation, as shown in Eq. (S11). From the permutation rule, the following Hermitian conjugate and decomposition/contraction rules can be directly derived.

Hermitian conjugate. The Hermitian conjugate of Grassmann tensor \mathbf{T} in Eq. (S14) is

$$\mathbf{T}^\dagger = \sum_{l_1 \dots l_r} \tilde{T}_{l_1 l_2 \dots l_r} \eta_{l_r}^{p(l_r)} \dots \eta_{l_{m+1}}^{p(l_{m+1})} \bar{\eta}_{l_m}^{p(l_m)} \dots \bar{\eta}_{l_1}^{p(l_1)}, \quad (\text{S16})$$

$$\tilde{T}_{l_1 l_2 \dots l_r} = (-1)^{\sum_{i=m+1}^r p(l_i)} T_{l_1 l_2 \dots l_r}^*. \quad (\text{S17})$$

Note that \mathbf{T} has a definite parity and thus $p(\mathbf{T}) = \sum_{i=1}^r p(l_i) \text{ mod } 2$.

We can motivate Eqs. (S16-S17). We know \mathbf{T}^\dagger should have the form Eq. (S16), and thus we only need to derive

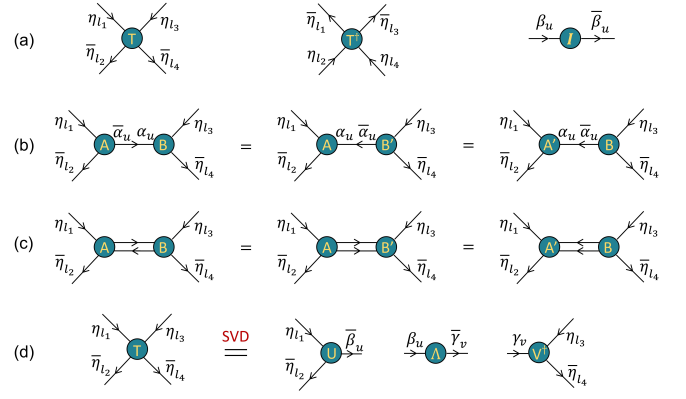


FIG. S1. Graphical notation for Grassmann tensors. Incoming and outgoing arrows correspond to Grassmann variables α and $\bar{\alpha}$, respectively. (a) Grassmann tensor \mathbf{T} and its Hermitian conjugate. (b) Grassmann tensor contractions for one common index. (c) Grassmann tensor contractions for two common indices with different arrow directions. (d) SVD for a Grassmann tensor.

Eq. (S17). We consider the scalar product $\int_{\text{all}} \mathbf{T}^\dagger \mathbf{T}$ (i.e. the norm of the Grassmann tensor), which is expected to be a real number $\sum_{l_1 l_2 \dots l_r} |T_{l_1 l_2 \dots l_r}|^2$ by integrating out all indices. On the other hand, according to Eq. (S12), we have $\int \bar{\eta}_{l_k}^{p(l_k)} \eta_{l_k}^{p(l_k)} = 1$ and $\int \eta_{l_k}^{p(l_k)} \bar{\eta}_{l_k}^{p(l_k)} = (-1)^{p(l_k)}$. It is easy to verify that $\int_{\text{all}} \mathbf{T}^\dagger \mathbf{T} = \sum_{l_1 l_2 \dots l_r} T_{l_1 l_2 \dots l_r} \tilde{T}_{l_1 l_2 \dots l_r} (-1)^{\sum_{i=m+1}^r p(l_i)}$, and thus we obtain Eq. (S16).

Using Eqs. (S16-S17), we derive the identity $\int_{\text{all}} \mathbf{T} \mathbf{T}^\dagger = \sum_{l_1 l_2 \dots l_r} |T_{l_1 l_2 \dots l_r}|^2 (-1)^{\sum_{i=1}^r p(l_i)} = (-1)^{p(\mathbf{T})} \int_{\text{all}} \mathbf{T}^\dagger \mathbf{T}$, where the total parity $p(\mathbf{T})$ determines the sign. This sign reversal arises because exchanging two odd-parity tensors ($p(\mathbf{T}) = 1$) introduces a factor of -1 , while even-parity tensors ($p(\mathbf{T}) = 0$) leave the integral invariant, thereby confirming the consistency of the conjugate relations. Additionally, the double conjugate satisfies $(\mathbf{T}^\dagger)^\dagger = (-1)^{p(\mathbf{T})} \mathbf{T}$. These observations suggest that handling even-parity Grassmann tensors is more convenient than their odd-parity counterparts.

As a convenient graphical notation, we assign an arrow to each tensor leg, shown in Fig. S1(a). The tensor legs with incoming arrows correspond to α (creation operator c^\dagger), and outgoing arrows correspond to $\bar{\alpha}$ (annihilation fermionic operator c). For its Hermitian conjugate \mathbf{T}^\dagger , we need to reverse the arrow direction for each leg, and modify the tensor elements by multiplying by the phase factor $(-1)^{p(l_i)}$ for each outgoing leg of \mathbf{T} according to Eq. (S17).

Decomposition and contraction. Here we first look at the rule of decomposition. Defining $\mathbf{T} = \sum_{l_1 \dots l_r} T_{l_1 \dots l_r} \eta_{l_1}^{p(l_1)} \dots \eta_{l_r}^{p(l_r)}$, then $T_{l_1 \dots l_r}$ can be decomposed as $T_{l_1 \dots l_r} = \sum_{uv} A_{l_1 \dots l_i, u} \delta_{uv} B_{v, l_{i+1} \dots l_r}$. According to Eq. (S12), using $\int \bar{\alpha}_u^{p(u)} \alpha_v^{p(v)} = \delta_{uv}$ (here $u = 0, 1, \dots, D-1$ distinguishes the D Grassmann variables and $p(u)$ is the corresponding parity and thus $\delta_{uv} = \delta_{p(u), p(v)}$), we have $\mathbf{T} = \int_{\alpha} \mathbf{A} \mathbf{B}$ (integrating out the α Grassmann variable), where

$$\begin{aligned}\mathbf{A} &= \sum_{l_1 \dots l_r, u} A_{l_1 \dots l_r, u} \eta_{l_1}^{p(l_1)} \dots \eta_{l_r}^{p(l_r)} \bar{\alpha}_u^{p(u)}, \\ \mathbf{B} &= \sum_{l_{r+1} \dots l_r, u} B_{u, l_{r+1} \dots l_r} \alpha_u^{p(u)} \eta_{l_{r+1}}^{p(l_{r+1})} \dots \eta_{l_r}^{p(l_r)}.\end{aligned}\quad (\text{S18})$$

Similarly, we can also use $\int \alpha_v^{p(v)} \bar{\alpha}_u^{p(u)} = (-1)^{p(u)} \delta_{uv}$ and absorb the phase factor $(-1)^{p(u)}$ into \mathbf{B} , and then we have $\mathbf{T} = \int_{\alpha} \mathbf{A} \mathbf{B}'$ where

$$\begin{aligned}\mathbf{A} &= \sum_{l_1 \dots l_r, u} A_{l_1 \dots l_r, u} \eta_{l_1}^{p(l_1)} \dots \eta_{l_r}^{p(l_r)} \alpha_u^{p(u)}, \\ \mathbf{B}' &= \sum_{l_{r+1} \dots l_r, u} (-1)^{p(u)} B_{u, l_{r+1} \dots l_r} \bar{\alpha}_u^{p(u)} \eta_{l_{r+1}}^{p(l_{r+1})} \dots \eta_{l_r}^{p(l_r)}.\end{aligned}\quad (\text{S19})$$

Of course, we can also absorb the phase factor $(-1)^{p(u)}$ into \mathbf{A} rather than \mathbf{B} , and then we have $\mathbf{T} = \int_{\alpha} \mathbf{A}' \mathbf{B}$ where

$$\begin{aligned}\mathbf{A}' &= \sum_{l_1 \dots l_r, u} (-1)^{p(u)} A_{l_1 \dots l_r, u} \eta_{l_1}^{p(l_1)} \dots \eta_{l_r}^{p(l_r)} \alpha_u^{p(u)}, \\ \mathbf{B} &= \sum_{l_{r+1} \dots l_r, u} B_{u, l_{r+1} \dots l_r} \bar{\alpha}_u^{p(u)} \eta_{l_{r+1}}^{p(l_{r+1})} \dots \eta_{l_r}^{p(l_r)}.\end{aligned}\quad (\text{S20})$$

Contraction can be viewed as the reverse of decomposition. Taking the Grassmann tensor $\mathbf{T} = \sum_{l_1 l_2 l_3 l_4} T_{l_1 l_2 l_3 l_4} \eta_{l_1}^{p(l_1)} \bar{\eta}_{l_2}^{p(l_2)} \eta_{l_3}^{p(l_3)} \bar{\eta}_{l_4}^{p(l_4)}$ as an example, the above three different decomposition forms in Eq. (S18), Eq. (S19) and Eq. (S20) respectively correspond to the contraction of two tensors, shown in Fig. S1(b). In practice, the tensor legs to be contracted may have different arrow directions, shown in Fig. S1(c). In this situation, we can arrange the arrows to have the same direction by modifying the tensor elements, according to Eq. (S19) or (S20).

The singular value decomposition (SVD) is another basic operation in tensor network computations. As an application, here we look into how to perform SVD. According to conventional SVD, we have $T_{l_1 l_2 l_3 l_4} = \sum_{uv} U_{l_1 l_2, u} \Lambda_{uv} (V^\dagger)_{v, l_3 l_4}$. Then the Grassmann SVD for $\mathbf{T} = \int_{\beta\gamma} \mathbf{U} \mathbf{A} \mathbf{V}^\dagger$ can be directly written down:

$$\begin{aligned}\mathbf{U} &= \sum_{l_1 l_2 u} U_{l_1 l_2, u} \eta_{l_1}^{p(l_1)} \bar{\eta}_{l_2}^{p(l_2)} \bar{\beta}_u^{p(u)} \\ \Lambda &= \sum_{uv} \Lambda_{uv} \beta_u^{p(u)} \bar{\gamma}_v^{p(v)} \\ \mathbf{V}^\dagger &= \sum_{v l_3 l_4} (V^\dagger)_{v, l_3 l_4} \gamma_v^{p(v)} \eta_{l_3}^{p(l_3)} \bar{\eta}_{l_4}^{p(l_4)}\end{aligned}\quad (\text{S21})$$

We find \mathbf{U} and \mathbf{V}^\dagger naturally satisfy the unitary property. Taking \mathbf{U} as an example, according to Eq. (S16) and the unitary properties of $U_{l_1 l_2, u}$, it is easy to verify that

$$\int_{\eta_1 \eta_2} \mathbf{U}^\dagger \mathbf{U} = (-1)^{p(\mathbf{U})} \int_{\eta_1 \eta_2} \mathbf{U} \mathbf{U}^\dagger = \sum_u \beta_u^{p(u)} \bar{\beta}_u^{p(u)}, \quad (\text{S22})$$

corresponding to the $D \times D$ identity Grassmann tensor where D is the number of Grassman variables ($u = 0, 1, \dots, D-1$), similar to Eq. (S12). The QR (LQ) decomposition can be performed in the same way.

Therefore, in practice, for Grassmann tensors, we only need do tensor contractions or decompositions on the tensor elements $T_{l_1 \dots l_r}$, and simultaneously consider possible phase factors arising from the anti-commutation relations. All these operations are local, and thus Grassmann tensors can be very conveniently dealt with like bosonic tensors.

C. Grassmann representation for fPEPS

Replacing fermionic operators by Grassmann variables, we can express Eq. (S1) and Eq. (S2) with their Grassmann forms:

$$\mathbf{G}_{ij} = \sum_{s=0}^{D-1} \eta_{X_i, s}^{p(s)} \eta_{X_j, s}^{p(s)} |0\rangle, \quad (\text{S23})$$

$$\mathbf{P}_i = \sum_{m_i} \sum_{l_{ur d=0}}^{D-1} T_{l_{ur d}^{[m_i]}} \bar{\eta}_{L_i, l}^{p(l)} \bar{\eta}_{U_i, u}^{p(u)} \bar{\eta}_{R_i, r}^{p(r)} \bar{\eta}_{D_i, d}^{p(d)}. \quad (\text{S24})$$

where $\bar{\eta}_{L_i, l}$ is the l -th Grassmann variable on the leg L_i (similar for others). The fPEPS wave function in its Grassmann representation is written as

$$|\Psi\rangle = \int_{\text{virtual}} \prod_i \mathbf{P}_i \prod_{\langle i, j \rangle} \mathbf{G}_{ij} |0\rangle, \quad (\text{S25})$$

where the subscript ‘‘virtual’’ means integrate over all the Grassmann variables on the virtual indices.

Assuming $\mathbf{T} = \sum_{l_1 \dots l_r} T_{l_1 \dots l_r} \eta_{l_1}^{p(l_1)} \dots \eta_{l_r}^{p(l_r)}$ can be decomposed as $T_{l_1 \dots l_r} = \sum_{uv} A_{l_1 \dots l_r, u} \delta_{uv} B_{v, l_{r+1} \dots l_r}$. Using $T_{l_1 \dots l_r} = \sum_{uvxy} A_{l_1 \dots l_r, u} \delta_{ux} \delta_{xy} \delta_{yv} B_{v, l_{r+1} \dots l_r}$, we have $\mathbf{T} = \int_{\alpha_u \beta_v} \mathbf{A} \mathbf{B} \mathbf{G}$, where

$$\begin{aligned}\mathbf{A} &= \sum_{l_1 \dots l_r, u} A_{l_1 \dots l_r, u} \eta_{l_1}^{p(l_1)} \dots \eta_{l_r}^{p(l_r)} \bar{\alpha}_u^{p(u)}, \\ \mathbf{B} &= \sum_{l_{r+1} \dots l_r, v} B_{v, l_{r+1} \dots l_r} \bar{\beta}_v^{p(v)} \eta_{l_{r+1}}^{p(l_{r+1})} \dots \eta_{l_r}^{p(l_r)}, \\ \mathbf{G} &= \sum_{xy} \delta_{xy} \beta_y^{p(y)} \alpha_x^{p(x)} = \sum_x \beta_x^{p(x)} \alpha_x^{p(x)}.\end{aligned}\quad (\text{S26})$$

Alternatively, we can absorb \mathbf{G} into \mathbf{A} or \mathbf{B} , to get other equivalent decomposition forms as given by Eq. (S18), Eq. (S19), or Eq. (S20). This indicates that in the fPEPS expression Eq. (S25), by absorbing \mathbf{G}_{ij} into \mathbf{P}_i , we can reexpress fPEPS as

$$|\Psi\rangle = \int_{\text{virtual}} \prod_i \mathbf{T}_i |0\rangle, \quad (\text{S27})$$

where \mathbf{T}_i has the same rank as \mathbf{P}_i .

In Fig. S2(a), we show the Grassmann tensor network representation for fPEPS. The arrow directions indicate the

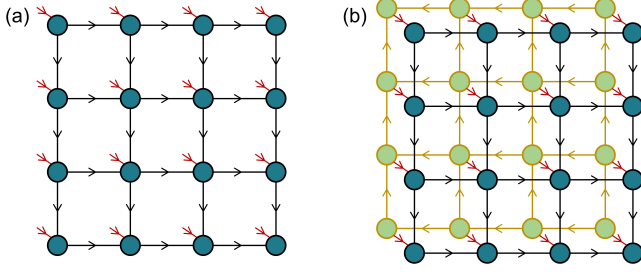


FIG. S2. (a) Grassmann tensor network representation of fPEPS $|\Psi\rangle$. (b) Double-layer grassmann tensor network representation of the fPEPS norm (squared) $\langle\Psi|\Psi\rangle$. Arrow directions indicate contraction orders between η and its conjugate $\bar{\eta}$.

contraction orders to sum over virtual fermions, which can be chosen arbitrarily at the very beginning. Its norm can be computed by integrating out the physical degrees of freedom:

$$\langle\Psi|\Psi\rangle = \int_{\text{virtual}} \prod_i \left(\int_{\text{physical}} \mathbf{T}_i^\dagger \mathbf{T}_i \right) |0\rangle, \quad (\text{S28})$$

where \mathbf{T}_i^\dagger is the Hermitian conjugate, obtained from Eq. (S16). The Grassmann tensor network for the norm is shown in Fig. S2(b), and it corresponds to a unique value.

D. Operators in Grassmann form

Now we consider the spinful fermionic operators c_σ^\dagger and c_σ for the Hubbard model as a specific example of using the Grassmann form. The local basis elements for one site respectively are $|0\rangle$, $|\uparrow\rangle$, $|\downarrow\rangle$ and $|\uparrow\downarrow\rangle$, and

$$\begin{aligned} c_\uparrow^\dagger &= |\uparrow\rangle\langle 0| + |\uparrow\downarrow\rangle\langle\downarrow|, \\ c_\uparrow &= |0\rangle\langle\uparrow| + |\downarrow\rangle\langle\uparrow\downarrow|, \\ c_\downarrow^\dagger &= |\downarrow\rangle\langle 0| - |\uparrow\downarrow\rangle\langle\uparrow|, \\ c_\downarrow &= |0\rangle\langle\downarrow| - |\uparrow\rangle\langle\uparrow\downarrow|. \end{aligned} \quad (\text{S29})$$

Now we use four Grassmann variables to denote the four bases, α_s ($s = 0, 1, 2, 3$) for the corresponding ket $|0\rangle$, $|\uparrow\rangle$, $|\downarrow\rangle$ and $|\uparrow\downarrow\rangle$, and $\bar{\xi}_t$ ($t = 0, 1, 2, 3$) for the corresponding bra $\langle 0|$, $\langle\uparrow|$, $\langle\downarrow|$ and $\langle\uparrow\downarrow|$. Thus we can express spinful fermionic operators as Grassmann tensors with dimension 4×4 . Taking c_\uparrow^\dagger as an example, $c_\uparrow^\dagger \doteq \sum_{st} A_{st} \alpha_s^{p(s)} \bar{\xi}_t^{p(t)}$, here $A_{st} = 0$ except for $(s, t) = (1, 0)$ which has $A_{10} = 1$, $p(s) = 1$ and $p(t) = 0$, and for $(s, t) = (3, 2)$ which has $A_{32} = 1$, $p(s) = 0$ and $p(t) = 1$. Here $p(s)$ and $p(t)$ count the parity of the electron number in the bases.

Furthermore, given $c_\uparrow \doteq \sum_{mn} B_{mn} \alpha_m^{p(m)} \bar{\xi}_n^{p(n)}$, the hopping term $c_{i,\uparrow}^\dagger c_{j,\uparrow}$ is expressed as:

$$\begin{aligned} c_{i,\uparrow}^\dagger c_{j,\uparrow} &\doteq \sum_{stmn} A_{st} B_{mn} \alpha_{i,s}^{p(s)} \bar{\xi}_{i,t}^{p(t)} \alpha_{j,m}^{p(m)} \bar{\xi}_{j,n}^{p(n)} \\ &= \sum_{stmn} (-1)^{p(t)*p(m)} A_{st} B_{mn} \alpha_{i,s}^{p(s)} \alpha_{j,m}^{p(m)} \bar{\xi}_{i,t}^{p(t)} \bar{\xi}_{j,n}^{p(n)}, \end{aligned} \quad (\text{S30})$$

where i and j denote the Grassmann variables on site i and j , respectively. Similarly we can express other operators including time evolution operators in the Grassmann form, and then we just need do Grassmann tensor operations to carry out fermionic tensor network computations.

II. fPEPS algorithms

Now we consider fPEPS computations on the Hubbard model. To fix the total electron number at N_e , we impose $U(1)$ symmetry on the local tensors [62, 63]. Below we consider two optimization schemes: the imaginary time evolution method, and the variational Monte Carlo method. The imaginary time evolution is conducted by the very efficient simple update method [27], to find the approximate ground state. The variational Monte Carlo scheme provides a different approach for optimization and computing physical quantities, with initial states from the simple update method.

A. simple update imaginary time evolution

According to the imaginary time evolution method, the ground state is found by

$$|\Psi_0\rangle = \lim_{\tau \rightarrow \infty} e^{-\tau H} = \lim_{N \rightarrow \infty} e^{-Nd\tau H}, \quad (\text{S31})$$

where $t = Nd\tau$. The Hubbard Hamiltonian contains a set of two-body interaction terms, i.e., $H = \sum_{\langle ij \rangle} h_{ij}$, and then the evolution operator can be expressed with the Suzuki-Trotter expansion:

$$e^{-d\tau H} = \prod_{\langle ij \rangle} e^{-d\tau h_{ij}} + O(\tau^2). \quad (\text{S32})$$

The simple update method provides an very efficient approach for performing the imaginary time evolution [27]. In this way, the two-site evolution operator $e^{-d\tau h_{ij}}$ only acts on the site tensor i and j , and the environmental effects from other sites are approximated by a series of diagonal matrices λ_i on the dangling bonds of the tensors. Note from Eq. (S30), the evolution operator has the following form:

$$e^{-d\tau h_{ij}} = \sum_{stmn} E_{stmn} \alpha_{i,s}^{p(s)} \alpha_{j,m}^{p(m)} \bar{\xi}_{i,t}^{p(t)} \bar{\xi}_{j,n}^{p(n)}. \quad (\text{S33})$$

Then the evolution operator acting on the fPEPS tensors is straightforward, which is graphically shown in Fig. S3. The SU is similar to that of bosonic/spin PEPS. It has a computational cost scaling as $O(D^5)$ by using QR/LQ decomposition for nearest neighbor interaction terms on the square lattice [66], as well as for next-nearest neighbor interactions [40], and thus allows us to reach a quite large bond dimensions D .

When using the SU method to update tensors, given the bond dimension D , we usually use an imaginary time step

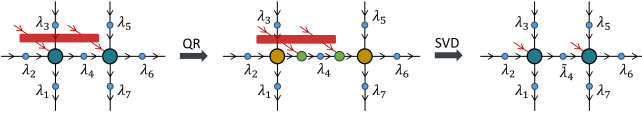


FIG. S3. Simple update imaginary time evolution operator for fPEPS. Environment tensors are approximated by diagonal matrices λ_i (blue circles), and are absorbed into tensors to be updated. Then the QR/LQ decomposition is done on the tensor pair, followed by a SVD on the subtensors (green circles) [66]. Please see Ref. [40] for a similar description with more details for spin PEPS.

$d\tau = 0.01$ until the fPEPS is converged, that is the environment tensors λ_i satisfy $\frac{1}{P} \sum_{i=1}^P \frac{\|\lambda_i(\tau+d\tau) - \lambda_i(d\tau)\|}{\lambda_i(\tau)} < 10^{-10}$. For spin models, when performing simple update, the large- D PEPS state is usually initialized from a converged PEPS with small D , while for fermionic models we find this tends to get trapped into a local minimum on 6×16 and 8×16 lattices. To escape this local minimum, we add pinning fields to target specified states.

For the $U(1)$ -charge symmetric fPEPS we consider here, we impose magnetic field terms $-h_i S_i^z$ ($|h_i| \sim 0.5$ and S_i^z is the spin- z component operator) or charge field terms $-\mu_i n_i$ ($\mu_i \sim 0.5$ and n_i is the particle number operator) in the Hamiltonian for the simple update. The pinning fields are imposed on sites chosen to get a desired magnetic pattern or charge pattern [3]. Taking the 8×16 lattice as an example, typically, we start from a random $D = 8$ state and perform simple update under pinning fields and then increase D directly from 8 to 16, and further to 28. For each given $D = 8, 16$ and 28, the simple update evolution is converged (i.e. λ_i is converged as mentioned above). Next we remove the pinning field and continue the simple update with $D = 28$ until convergence again. This fPEPS $D = 28$ state is regarded as the stable state. With this $D = 28$ state, we can get smaller- D fPEPS state in a reverse process, i.e., by gradually decreasing D from 28 to smaller values through simple update and simultaneously ensuring λ_i convergence for each D .

B. Variational Monte Carlo

In variational Monte Carlo, the energy function is expressed as

$$E = \frac{\langle \Psi | H | \Psi \rangle}{\langle \Psi | \Psi \rangle} = \frac{1}{Z} \sum_{\mathbf{k}} |\Psi(\mathbf{k})|^2 E_{\text{loc}}(\mathbf{k}) \doteq \langle E_{\text{loc}}(\mathbf{k}) \rangle, \quad (\text{S34})$$

where $\Psi(\mathbf{k})$ is the amplitude of configuration $|\mathbf{k}\rangle = |k_1 k_2 \dots k_N\rangle$, and

$$E_{\text{loc}}(\mathbf{k}) = \sum_{\mathbf{k}'} \frac{\Psi(\mathbf{k}')}{\Psi(\mathbf{k})} \langle \mathbf{k} | H | \mathbf{k}' \rangle. \quad (\text{S35})$$

The amplitude $\Psi(\mathbf{k})$ is computed through the standard boundary-MPS contraction method [23, 40]. Note $\langle \dots \rangle$ in Eq.(S34) denotes the Monte Carlo (MC) average.

Additionally, the energy gradients with respect to the tensor elements are

$$g_p = 2 \langle E_{\text{local}}(\mathbf{k}) O_p(\mathbf{k}) \rangle - 2 \langle E_{\text{local}}(\mathbf{k}) \rangle \langle O_p(\mathbf{k}) \rangle \quad (\text{S36})$$

where $O_p(\mathbf{k}) = \frac{1}{\Psi(\mathbf{k})} \Delta_p^\dagger(\mathbf{k})$, and $\Delta_p(\mathbf{k})$ is obtained by contracting a single-layer tensor network with the configuration $|\mathbf{k}\rangle$ except for the element at the corresponding position p [40], and $\Delta_p^\dagger(\mathbf{k})$ is its Hermitian conjugate defined as in Eq. (S16).

1. Monte Carlo sampling procedure

In the MC sampling, we sample the configurations in the subspace $N_\uparrow = N_\downarrow = \frac{1}{2} N_e$, where N_\uparrow (N_\downarrow) is the number of spin-up (down) particles. This is equivalent to enforcing $U(1) \times U(1)$ symmetry on the wave function. The configurations are generated using Metropolis' algorithm. Specifically, assuming the current configuration is $|\mathbf{k}_a\rangle = |k_1 \dots k_i k_{i+1} \dots k_N\rangle$ satisfying $N_\uparrow = N_\downarrow = \frac{1}{2} N_f$, we propose a trial configuration $|\mathbf{k}_b\rangle = |k_1 \dots k'_i k'_{i+1} \dots k_N\rangle$ obtained by flipping the states on a nearest-neighbor pair of site i and $i+1$, to be accepted according to Metropolis' algorithm. To generate configurations quickly, we loop over the rows and attempt to flip each pair according to the Metropolis acceptance criterion [40]:

$$P = \min \left[1, \frac{|\Psi(\mathbf{k}_b)|^2}{|\Psi(\mathbf{k}_a)|^2} \right]. \quad (\text{S37})$$

The trial configuration $|\mathbf{k}_b\rangle$ will be accepted as a new configuration if a randomly chosen number from the uniform distribution in the interval $[0,1)$ is smaller than the probability P . Otherwise, the trial configuration $|\mathbf{k}_b\rangle$ is rejected, and another trial configuration $|\mathbf{k}'_b\rangle$ is considered. To keep $N_\uparrow = N_\downarrow = \frac{1}{2} N_e$, the trial states are constrained. For example, if the current states on sites i and $i+1$ are $|\uparrow_i, \downarrow_{i+1}\rangle$, then the trial states $|k'_i k'_{i+1}\rangle$ can only be $|\uparrow_i \downarrow_{i+1}, 0_{i+1}\rangle$, $|0_i, \uparrow_{i+1} \downarrow_{i+1}\rangle$, or $|\downarrow_i, \uparrow_{i+1}\rangle$. A Monte Carlo sweep is defined as a sweep over all horizontal and vertical nearest-neighbor pairs through the lattice, and the physical quantities are measured after each Monte Carlo sweep.

2. Stochastic optimization

The energy gradients can be evaluated via Monte Carlo sampling, and thus it is natural to optimize the fPEPS by gradient methods. We consider two gradient-based methods: stochastic gradient descent (SGD) [36, 40, 64] and stochastic reconfiguration (SR) [69–71].

For SGD, tensor elements are updated following the (negative) of their gradients:

$$x_p(\tau + 1) = x_p(\tau) - r_p \cdot d\tau \cdot \text{sgn}(g_p), \quad (\text{S38})$$

where τ is the number of optimization steps, and r_p is an independent random number in the interval $(0,1)$ for each

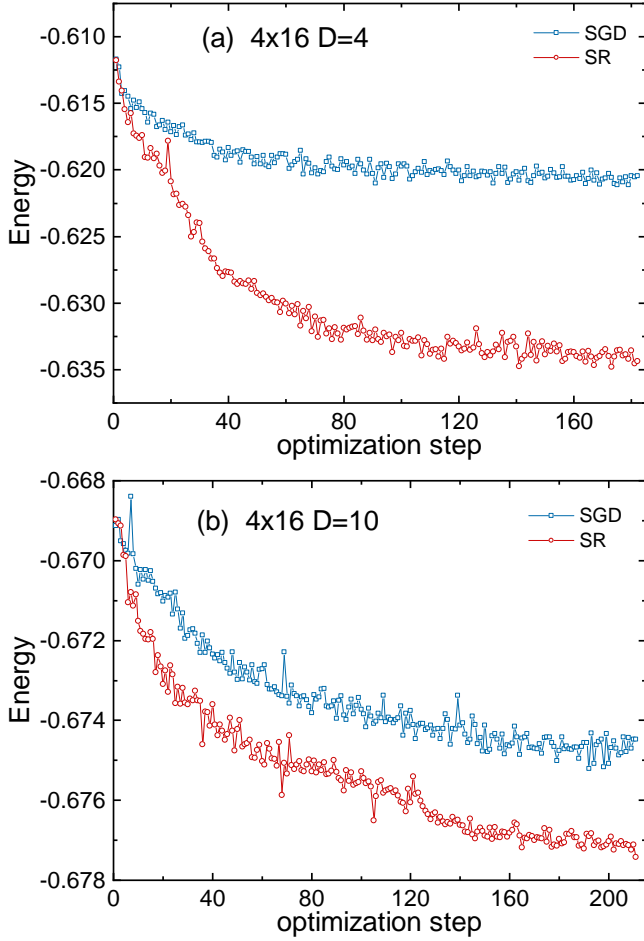


FIG. S4. Gradient-based optimization of energy with SGD and SR methods, for the 4×16 $U = 8$ Hubbard model with $N_e = 56$ electrons, using fPEPS (a) $D = 4$ and (b) $D = 10$.

tensor element x_p . The parameter $d\tau$ is the step size, setting the variation range for an element. Starting from the simple update state, the step length $d\tau$ can be gradually tuned from 0.005 to a smaller one like 0.001 [40].

For SR, it optimizes the tensors on the fPEPS manifold, which is equivalent to the imaginary time evolution using the time-dependent variational principle [69]. In this method, we need to solve a system of linear equations:

$$\sum_q S_{pq} \dot{x}_q = g_p, \quad (\text{S39})$$

where $S_{pq} = \langle O_p(\mathbf{k}) O_q(\mathbf{k}) \rangle - \langle O_p(\mathbf{k}) \rangle \langle O_q(\mathbf{k}) \rangle$. To avoid explicitly constructing the \mathbf{S} matrix, we solve the above equation in an iterative way [70], and we only need to know how to map a vector $\dot{\mathbf{x}}$ to \mathbf{y} under the action of \mathbf{S} to realize $\mathbf{y} = \mathbf{S}\dot{\mathbf{x}}$. Specifically,

$$y_p = \sum_n S_{pn} \dot{x}_n = y_p^{(1)} - y_p^{(2)},$$

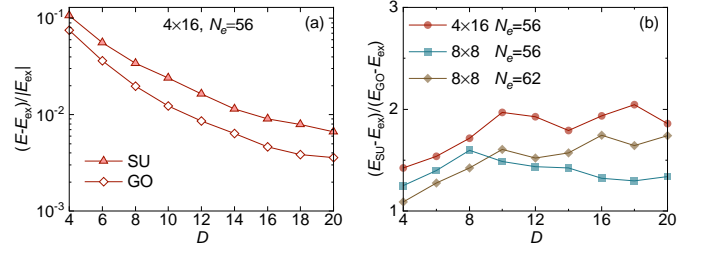


FIG. S5. (a) The relative energy errors of SU and GO results with respect to D for the 4×16 Hubbard model at $U = 8$ with electron numbers $N_e = 56$. The extrapolated DMRG energy is used for the reference. (b) The ratio between the SU energy error and the GO energy error for each bond dimension D for various systems.

where

$$y_p^{(1)} = \frac{1}{N_{\text{MC}}} \sum_{\mathbf{k}} O_p(\mathbf{k}) \left[\sum_q O_q(\mathbf{k}) x_q \right],$$

$$y_p^{(2)} = \langle O_p(\mathbf{k}) \rangle \sum_q \langle O_q(\mathbf{k}) \rangle x_q,$$

where $\langle O_p(\mathbf{k}) \rangle \equiv \frac{1}{N_{\text{MC}}} \sum_{\mathbf{k}} O_p(\mathbf{k})$ is the Monte Carlo average of $O_p(\mathbf{k})$, and N_{MC} is the number of Monte Carlo sweeps. Note $O_p(\mathbf{k})$ can be stored trivially on different CPU processors, while still being convenient to iteratively solve Eq. (S39) (a diagonal shift 0.001 for regularizing the \mathbf{S} matrix is also added). Once we obtain the solution \dot{x}_p , the tensor elements are updated as

$$x_p(\tau + 1) = x_p(\tau) - d\tau \cdot \dot{x}_p, \quad (\text{S40})$$

where $d\tau$ is the step size, which can be tuned from $d\tau = 0.05$ to 0.01.

In Fig. S4, we show the energy variation with respect to the optimization step by SGD and SR methods for the 4×16 lattice with Hubbard interaction $U = 8$ at hole doping $n_h = 0.125$, using fPEPS $D = 4$ and $D = 10$. For all cases, we start from the states from the simple update method, and the number of Monte Carlo sweeps for each optimization step is about 20000. The step size is adjusted from 0.005 to 0.001 for SGD and from 0.05 to 0.01 for SR according to the energy behavior, ensuring good optimization performance. Clearly, for both $D = 4$ and $D = 10$, the SR method works better than the SGD method. Therefore, all of the results presented from gradient-based optimization (GO) use the SR optimization.

3. Accuracy comparison of gradient optimization and simple update

Now we compare the accuracy of the energy obtained from gradient optimization and simple update. In Fig. S5(a), we show the energies from SU and GO methods. For SU, the energy relative error can be as small as 0.0055 with $D = 20$. With SU states as starting points, GO can further improve the accuracy, for example, with the error going down to 0.0037 for $D = 20$. By comparing the energy errors between the GO

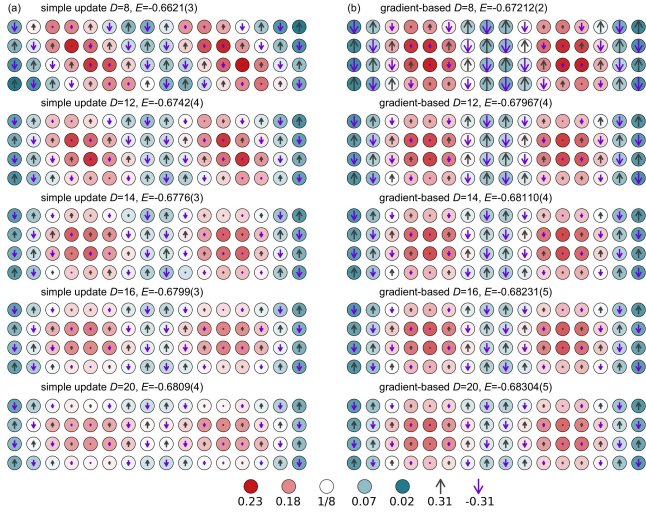


FIG. S6. The charge and spin pattern on 4×16 with $U = 8$ and $N_e = 56$. The left part shows the results obtained from the simple update, and the right is from gradient-based optimization. For the same D , gradient-based optimization is initialized by the simple update fPEPS state.

and SU methods for various bond dimensions D on different system sizes $L_y \times L_x$ including 4×16 and 8×8 , we find that the energy error of SU is only twice as large as that of GO, as shown in Fig. S5(b).

Meanwhile, we observe that both SU and GO yield nearly identical patterns of physical quantities for large D , as shown in Fig. S6 for 4×16 and Fig. S7 for 8×8 , with only slight quantitative differences. These findings suggest SU with large- D is able to converge essential aspects of physics.

4. Monte Carlo convergence and contraction convergence

Now we consider the convergence behaviour of MC sampling, as well as of the cutoff χ_s used for contracting single-layer tensor networks (the amplitude of a configuration) by the boundary-MPS method. Here we take the 8×8 Hubbard model with $U = 8$ and $N_e = 56$ as an example, using the fPEPS $D = 20$ ground state. Fig. S9(a) and (b) show the energy convergence behavior with respect to MC sweeps and χ_s , respectively. For a given large χ_s presented in Fig. S9(a), we can see the energy (persite) can be well evaluated by around 10000 MC sweeps, with an statistical error smaller than 3×10^{-4} .

As another example we consider the 8×16 Hubbard model with $U = 8$ and $N_e = 112$, using fPEPS $D = 24$. For the case 8×8 , it has been shown $\chi_s = 3D = 60$ is enough to converge the energy [Fig. S8(a)]. Here we consider larger χ_s with $\chi_s = 4D = 96$ and $\chi_s = 5D = 120$ for 8×16 , and it shows $\chi_s = 4D$ is good for convergence. Additionally, 10000 MC sweeps also work well to have a small statistical error about 3×10^{-4} .

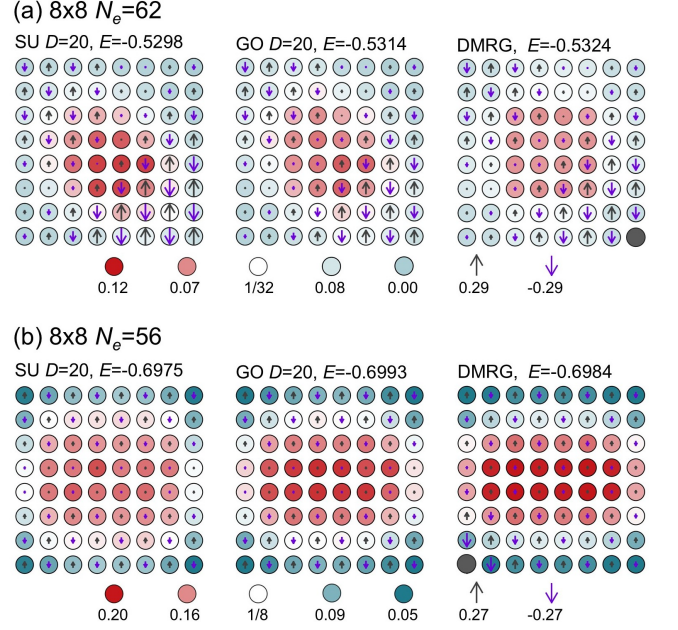


FIG. S7. The charge and spin pattern on the 8×8 lattice with $U = 8$ and (a) $N_e = 62$ and (b) $N_e = 56$. From left to right, the results are respectively obtained from the simple update (SU), gradient-based optimization (GO), and SU(2)-DMRG with $m = 32000$. For DMRG results, local spin z -component moments are zero due to SU(2) symmetry, and the presented arrows denote the spin correlation values $|\langle \mathbf{S}_{\text{ref}}^z \cdot \mathbf{S}_{i,j}^z \rangle|^{1/2}$ using the reference site (filled black circles), and each arrow direction (up or down) depends on the sign of $\langle \mathbf{S}_{\text{ref}}^z \cdot \mathbf{S}_{i,j}^z \rangle$.

III. Pattern evolution with bond dimension D

In Fig. S6, we have shown how the pattern evolves with respect to the fPEPS bond dimension D . Here we consider the case of 8×16 at hole doping $n_h = 1/8$ at $U = 8$. In Fig. S10, we show the pattern evolution for the diagonal, vertical and horizontal stripes. In each case, small- D results exhibit apparently ordered patterns. Increasing D , the orders are softened due to more quantum fluctuations being included in the fPEPS ansatz. For larger sizes, the patterns show a similar evolution of features as a function of D .

* wylu@zju.edu.cn

† gkc1000@gmail.com

- [1] J. Hubbard, "Electron correlations in narrow energy bands," *Proc. R. Soc. Lond. A* **276**, 238–257 (1963).
- [2] J. P. F. LeBlanc, Andrey E. Antipov, Federico Becca, Ireneusz W. Bulik, Garnet Kin-Lic Chan, Chia-Min Chung, Youjin Deng, Michel Ferrero, Thomas M. Henderson, Carlos A. Jiménez-Hoyos, E. Kozik, Xuan-Wen Liu, Andrew J. Millis, N. V. Prokof'ev, Mingpu Qin, Gustavo E. Scuseria, Hao Shi, B. V. Svistunov, Luca F. Tocchio, I. S. Tupitsyn, Steven R. White, Shiwei Zhang, Bo-Xiao Zheng, Zhenyue Zhu, and Emanuel Gull (Simons Collaboration on the Many-Electron

TABLE I. fPEPS and DMRG energies persite for 4×4 at half filling ($N_e = 16$) and $n_h = 1/8$ hole doping ($N_e = 14$) at Hubbard repulsive interaction $U = 8$. For DMRG results, the truncated weights for bond dimension $m = 2500$ are 4.12×10^{-9} and 7.55×10^{-8} for half-filling and $n_h = 1/8$, respectively. DMRG results with $m = \infty$ denote extrapolated energies using truncated weights.

4×4 , half-filling					4×4 , $n_h = 1/8$				
D	fPEPS-SU	fPEPS-GO	m	DMRG	D	fPEPS-SU	fPEPS-GO	m	DMRG
4	-0.4174(2)	-0.42115(3)	500	-0.42551504	4	-0.5497(6)	-0.5892(2)	500	-0.63241788
6	-0.4204(6)	-0.42416(7)	1000	-0.42552519	6	-0.5850(4)	-0.61225(7)	1000	-0.63260460
8	-0.4238(5)	-0.42508(4)	1500	-0.42552583	8	-0.6016(3)	-0.62314(6)	1500	-0.63261660
10	-0.4236(3)	-0.425429(8)	2000	-0.42552589	10	-0.6104(4)	-0.62725(4)	2000	-0.63261805
12	-0.4241(3)	-0.425493(3)	2500	-0.42552590	12	-0.6125(5)	-0.63159(3)	2500	-0.63261830
14	-0.4242(5)	-0.425508(5)	∞	-0.42552596(1)	14	-0.6154(4)	-0.63206(1)	∞	-0.6326190(1)
16	-0.4244(2)	-0.425519(6)			16	-0.6152(4)	-0.63234(2)		

TABLE II. fPEPS and DMRG energies persite for the Hubbard model at $U = 8$. For 6×6 , truncated weights from $m = 24000$ for $n_h = 1/18$ ($N_e = 34$) and $n_h = 1/9$ ($N_e = 32$) are 6.01×10^{-6} and 3.26×10^{-5} , respectively. For 4×16 , truncated weights from $m = 12000$ is 1.01×10^{-5} . DMRG results with $m = \infty$ denote extrapolated energies from truncated weights, not using the results from the presented maximal bond dimensions.

6×6 , $n_h = 1/18$					6×6 , $n_h = 1/9$					4×16 , $n_h = 1/8$				
D	fPEPS-SU	fPEPS-GO	m	DMRG	D	fPEPS-SU	fPEPS-GO	m	DMRG	D	fPEPS-SU	fPEPS-GO	m	DMRG
4	-0.5132(5)	-0.5273(3)	16000	-0.5598359	4	-0.5786(4)	-0.6007(7)	16000	-0.6570640	4	-0.6120(8)	-0.63383(4)	8000	-0.6852680
6	-0.5363(3)	-0.5448(1)	18000	-0.5598593	6	-0.6200(6)	-0.6309(4)	18000	-0.6571482	6	-0.6473(4)	-0.66062(6)	9000	-0.6853034
8	-0.5438(5)	-0.5509(1)	20000	-0.5598766	8	-0.6312(5)	-0.6415(2)	20000	-0.6572133	8	-0.6621(3)	-0.67212(2)	10000	-0.6853307
10	-0.5486(2)	-0.5542(2)	22000	-0.5598898	10	-0.6388(5)	-0.6448(2)	22000	-0.6572647	10	-0.6690(4)	-0.67712(5)	11000	-0.6853523
12	-0.5510(4)	-0.5561(2)	24000	-0.5599001	12	-0.6423(3)	-0.6485(1)	24000	-0.6573063	12	-0.6742(4)	-0.67967(4)	12000	-0.6853698
14	-0.5528(3)	-0.55766(7)	∞	-0.559969(16)	14	-0.6455(3)	-0.6513(2)	∞	-0.657675(82)	14	-0.6776(2)	-0.68110(4)	∞	-0.685544(38)
16	-0.5531(4)	-0.55827(3)			16	-0.6470(4)	-0.65327(5)			16	-0.6799(3)	-0.68231(5)		
18	-0.5539(2)	-0.55880(8)			18	-0.6475(3)	-0.65383(6)			18	-0.6803(3)	-0.68272(2)		
20	-0.5542(2)	-0.55908(7)			20	-0.6477(2)	-0.65475(8)			20	-0.6809(4)	-0.68304(5)		

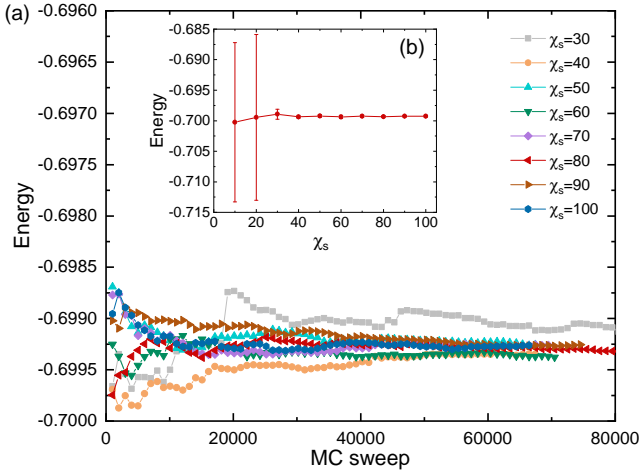


FIG. S8. For the 8×8 Hubbard model at $U = 8$ and $N_e = 56$ using fPEPS $D = 20$, the energy convergence behavior with respect to (a) MC sampling for different cutoff χ_s , and (b) cutoff χ_s with maximal samples from MC, and error bars are mean standard errors which are evaluated from multiple bins from MC sampling, in which each bin contains 10000 samples.

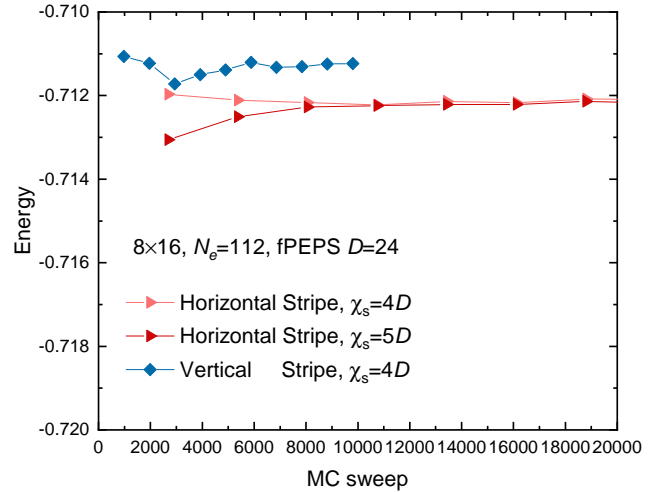


FIG. S9. Energy convergence with respect to MC sampling on the 8×16 Hubbard model at $N_e = 112$ and $U = 8$, for the horizontal stripe state with cutoff $\chi_s = 96$ (light red) and $\chi_s = 120$ (dark red), and vertical stripe state with $\chi_s = 96$ (blue).

Problem), “Solutions of the two-dimensional Hubbard model: Benchmarks and results from a wide range of numerical algorithms,” *Phys. Rev. X* **5**, 041041 (2015).

[3] Bo-Xiao Zheng, Chia-Min Chung, Philippe Corboz, Georg Ehlers, Ming-Pu Qin, Reinhard M. Noack, Hao Shi, Steven R. White, Shiwei Zhang, and Garnet Kin-Lic Chan, “Stripe order in the underdoped region of the two-dimensional Hubbard model,” *Science* **358**, 1155–1160 (2017).

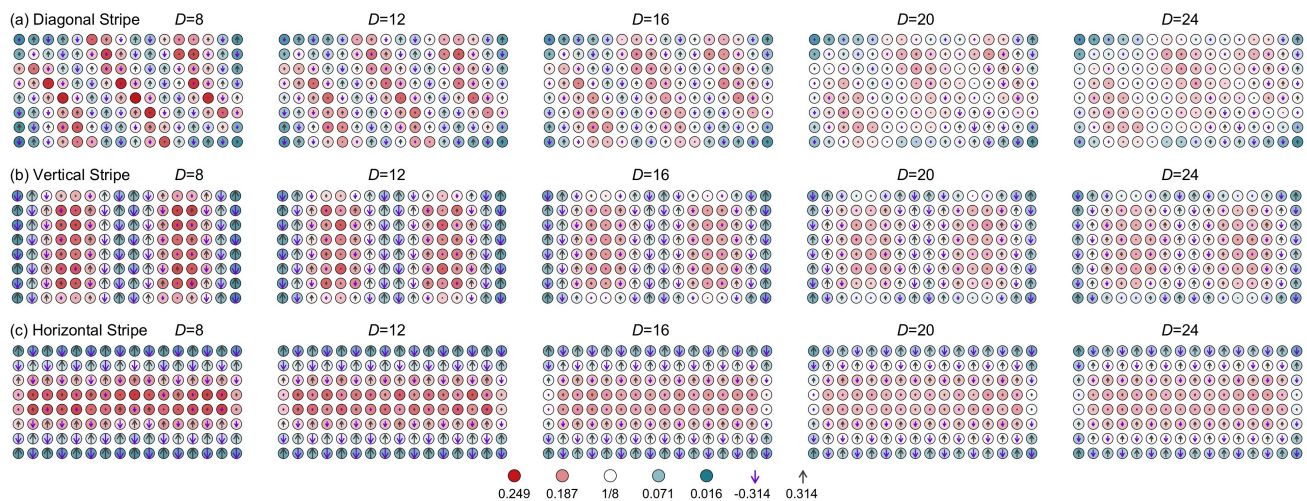


FIG. S10. The hole density and spin distribution on the 8×16 Hubbard model with $U = 8$ and $N_e = 112$, from fPEPS with different bond dimensions D .

- [4] Edwin W Huang, Ryan Sheppard, Brian Moritz, and Thomas P Devereaux, “Strange metallicity in the doped Hubbard model,” *Science* **366**, 987–990 (2019).
- [5] Hong-Chen Jiang and Thomas P. Devereaux, “Superconductivity in the doped Hubbard model and its interplay with next-nearest hopping t' ,” *Science* **365**, 1424–1428 (2019).
- [6] Mingpu Qin, Chia-Min Chung, Hao Shi, Ettore Vitali, Claudius Hubig, Ulrich Schollwöck, Steven R. White, and Shiwei Zhang (Simons Collaboration on the Many-Electron Problem), “Absence of superconductivity in the pure two-dimensional Hubbard model,” *Phys. Rev. X* **10**, 031016 (2020).
- [7] Hao Xu, Chia-Min Chung, Mingpu Qin, Ulrich Schollwöck, Steven R. White, and Shiwei Zhang, “Coexistence of superconductivity with partially filled stripes in the Hubbard model,” *Science* **384**, eadh7691 (2024).
- [8] Fedor Šimkovic IV, Riccardo Rossi, Antoine Georges, and Michel Ferrero, “Origin and fate of the pseudogap in the doped Hubbard model,” *Science* **385**, eade9194 (2024).
- [9] Elbio Dagotto, “Correlated electrons in high-temperature superconductors,” *Rev. Mod. Phys.* **66**, 763–840 (1994).
- [10] N. Bulut, “ $d_{x^2-y^2}$ superconductivity and the Hubbard model,” *Advances in Physics* **51**, 1587–1667 (2002).
- [11] D. J. Scalapino, “A common thread: The pairing interaction for unconventional superconductors,” *Rev. Mod. Phys.* **84**, 1383–1417 (2012).
- [12] Daniel P. Arovas, Erez Berg, Steven A. Kivelson, and Srinivas Raghu, “The Hubbard Model,” *Annual Review of Condensed Matter Physics* **13**, 239–274 (2022).
- [13] Mingpu Qin, Thomas Schäfer, Sabine Andergassen, Philippe Corboz, and Emanuel Gull, “The Hubbard Model: A Computational Perspective,” *Annual Review of Condensed Matter Physics* **13**, 275–302 (2022).
- [14] Daniel Greif, Maxwell F. Parsons, Anton Mazurenko, Christie S. Chiu, Sebastian Blatt, Florian Huber, Geoffrey Ji, and Markus Greiner, “Site-resolved imaging of a fermionic mott insulator,” *Science* **351**, 953–957 (2016).
- [15] Lawrence W. Cheuk, Matthew A. Nichols, Katherine R. Lawrence, Melih Okan, Hao Zhang, Ehsan Khatami, Nandini Trivedi, Thereza Paiva, Marcos Rigol, and Martin W. Zwierlein, “Observation of spatial charge and spin correlations in the 2D Fermi-Hubbard model,” *Science* **353**, 1260–1264 (2016).
- [16] Anton Mazurenko, Christie S. Chiu, Geoffrey Ji, Maxwell F. Parsons, Márton Kanász-Nagy, Richard Schmidt, Fabian Grusdt, Eugene Demler, Daniel Greif, and Markus Greiner, “A cold-atom Fermi-Hubbard antiferromagnet,” *Nature* **545**, 462–466 (2017).
- [17] Pimonpan Sompert, Sarah Hirthe, Dominik Bourgund, Thomas Chalopin, Julian Bibo, Joannis Koepsell, Petar Bojović, Ruben Verresen, Frank Pollmann, Guillaume Salomon, *et al.*, “Realizing the symmetry-protected haldane phase in Fermi-Hubbard ladders,” *Nature* **606**, 484–488 (2022).
- [18] Dominik Bourgund, Thomas Chalopin, Petar Bojović, Henning Schlömer, Si Wang, Titus Franz, Sarah Hirthe, Annabelle Bohrdt, Fabian Grusdt, Immanuel Bloch, *et al.*, “Formation of individual stripes in a mixed-dimensional cold-atom Fermi-Hubbard system,” *Nature* **637**, 57–62 (2025).
- [19] Danfeng Li, Kyuho Lee, Bai Yang Wang, Motoki Osada, Samuel Crossley, Hye Ryoung Lee, Yi Cui, Yasuyuki Hikita, and Harold Y Hwang, “Superconductivity in an infinite-layer nickelate,” *Nature* **572**, 624–627 (2019).
- [20] Motoharu Kitatani, Liang Si, Oleg Janson, Ryotaro Arita, Zhicheng Zhong, and Karsten Held, “Nickelate superconductors—a renaissance of the one-band Hubbard model,” *npj Quantum Materials* **5**, 59 (2020).
- [21] Steven R. White, “Density matrix formulation for quantum renormalization groups,” *Phys. Rev. Lett.* **69**, 2863–2866 (1992).
- [22] Frank Verstraete and J. Ignacio Cirac, “Renormalization algorithms for quantum-many body systems in two and higher dimensions,” *arXiv:cond-mat/0407066* (2004).
- [23] F. Verstraete, V. Murg, and J. I. Cirac, “Matrix product states, projected entangled pair states, and variational renormalization group methods for quantum spin systems,” *Advances in Physics* **57**, 143–224 (2008).
- [24] Christina V. Kraus, Norbert Schuch, Frank Verstraete, and J. Ignacio Cirac, “Fermionic projected entangled pair states,” *Phys. Rev. A* **81**, 052338 (2010).
- [25] Mark Fannes, Bruno Nachtergaele, and Reinhard F Werner, “Finitely correlated states on quantum spin chains,” *Commun. Math. Phys.* **144**, 443–490 (1992).

- [26] J. Jordan, R. Orús, G. Vidal, F. Verstraete, and J. I. Cirac, “Classical simulation of infinite-size quantum lattice systems in two spatial dimensions,” *Phys. Rev. Lett.* **101**, 250602 (2008).
- [27] H. C. Jiang, Z. Y. Weng, and T. Xiang, “Accurate determination of tensor network state of quantum lattice models in two dimensions,” *Phys. Rev. Lett.* **101**, 090603 (2008).
- [28] Román Orús and Guifré Vidal, “Simulation of two-dimensional quantum systems on an infinite lattice revisited: Corner transfer matrix for tensor contraction,” *Phys. Rev. B* **80**, 094403 (2009).
- [29] Ho N. Phien, Johann A. Bengua, Hoang D. Tuan, Philippe Corboz, and Román Orús, “Infinite projected entangled pair states algorithm improved: Fast full update and gauge fixing,” *Phys. Rev. B* **92**, 035142 (2015).
- [30] Philippe Corboz, “Variational optimization with infinite projected entangled-pair states,” *Phys. Rev. B* **94**, 035133 (2016).
- [31] Laurens Vanderstraeten, Jutho Haegeman, Philippe Corboz, and Frank Verstraete, “Gradient methods for variational optimization of projected entangled-pair states,” *Phys. Rev. B* **94**, 155123 (2016).
- [32] Ji-Yao Chen, Laurens Vanderstraeten, Sylvain Capponi, and Didier Poilblanc, “Non-abelian chiral spin liquid in a quantum antiferromagnet revealed by an ipeps study,” *Phys. Rev. B* **98**, 184409 (2018).
- [33] Hai-Jun Liao, Jin-Guo Liu, Lei Wang, and Tao Xiang, “Differentiable programming tensor networks,” *Phys. Rev. X* **9**, 031041 (2019).
- [34] Patrick C. G. Vlaar and Philippe Corboz, “Efficient tensor network algorithm for layered systems,” *Phys. Rev. Lett.* **130**, 130601 (2023).
- [35] Michael Lubasch, J. Ignacio Cirac, and Mari-Carmen Bañuls, “Algorithms for finite projected entangled pair states,” *Phys. Rev. B* **90**, 064425 (2014).
- [36] Wen-Yuan Liu, Shao-Jun Dong, Yong-Jian Han, Guang-Can Guo, and Lixin He, “Gradient optimization of finite projected entangled pair states,” *Phys. Rev. B* **95**, 195154 (2017).
- [37] Shao-Jun Dong, Chao Wang, Yongjian Han, Guang-can Guo, and Lixin He, “Gradient optimization of fermionic projected entangled pair states on directed lattices,” *Phys. Rev. B* **99**, 195153 (2019).
- [38] Reza Haghshenas, Matthew J. O’Rourke, and Garnet Kin-Lic Chan, “Conversion of projected entangled pair states into a canonical form,” *Phys. Rev. B* **100**, 054404 (2019).
- [39] Michael P. Zaletel and Frank Pollmann, “Isometric tensor network states in two dimensions,” *Phys. Rev. Lett.* **124**, 037201 (2020).
- [40] Wen-Yuan Liu, Yi-Zhen Huang, Shou-Shu Gong, and Zheng-Cheng Gu, “Accurate simulation for finite projected entangled pair states in two dimensions,” *Phys. Rev. B* **103**, 235155 (2021).
- [41] Johnnie Gray and Garnet Kin-Lic Chan, “Hyperoptimized approximate contraction of tensor networks with arbitrary geometry,” *Phys. Rev. X* **14**, 011009 (2024).
- [42] Wen-Yuan Liu, Si-Jing Du, Ruoqing Peng, Johnnie Gray, and Garnet Kin-Lic Chan, “Tensor network computations that capture strict variationality, volume law behavior, and the efficient representation of neural network states,” *Phys. Rev. Lett.* **133**, 260404 (2024).
- [43] Wen-Yuan Liu, Shou-Shu Gong, Yu-Bin Li, Didier Poilblanc, Wei-Qiang Chen, and Zheng-Cheng Gu, “Gapless quantum spin liquid and global phase diagram of the spin-1/2 $J_1 - J_2$ square antiferromagnetic Heisenberg model,” *Science Bulletin* **67**, 1034–1041 (2022).
- [44] Wen-Yuan Liu, Juraj Hasik, Shou-Shu Gong, Didier Poilblanc, Wei-Qiang Chen, and Zheng-Cheng Gu, “Emergence of gapless quantum spin liquid from deconfined quantum critical point,” *Phys. Rev. X* **12**, 031039 (2022).
- [45] Wen-Yuan Liu, Shou-Shu Gong, Wei-Qiang Chen, and Zheng-Cheng Gu, “Emergent symmetry in quantum phase transition: From deconfined quantum critical point to gapless quantum spin liquid,” *Science Bulletin* **69**, 190–196 (2024).
- [46] Wen-Yuan Liu, Didier Poilblanc, Shou-Shu Gong, Wei-Qiang Chen, and Zheng-Cheng Gu, “Tensor network study of the spin- $\frac{1}{2}$ square-lattice $J_1 - J_2 - J_3$ model: Incommensurate spiral order, mixed valence-bond solids, and multicritical points,” *Phys. Rev. B* **109**, 235116 (2024).
- [47] Wen-Yuan Liu, Xiao-Tian Zhang, Zhe Wang, Shou-Shu Gong, Wei-Qiang Chen, and Zheng-Cheng Gu, “Quantum criticality with emergent symmetry in the extended shastry-sutherland model,” *Phys. Rev. Lett.* **133**, 026502 (2024).
- [48] Philippe Corboz, Román Orús, Bela Bauer, and Guifré Vidal, “Simulation of strongly correlated fermions in two spatial dimensions with fermionic projected entangled-pair states,” *Phys. Rev. B* **81**, 165104 (2010).
- [49] Philippe Corboz, Steven R. White, Guifré Vidal, and Matthias Troyer, “Stripes in the two-dimensional t - J model with infinite projected entangled-pair states,” *Phys. Rev. B* **84**, 041108 (2011).
- [50] Philippe Corboz, T. M. Rice, and Matthias Troyer, “Competing states in the t - J model: Uniform d -wave state versus stripe state,” *Phys. Rev. Lett.* **113**, 046402 (2014).
- [51] Shao-Jun Dong, Chao Wang, Yong-Jian Han, Chao Yang, and Lixin He, “Stable diagonal stripes in the t - J model at $\bar{n}_h = 1/8$ doping from fPEPS calculations,” *npj Quantum Materials* **5**, 28 (2020).
- [52] Philippe Corboz, “Improved energy extrapolation with infinite projected entangled-pair states applied to the two-dimensional Hubbard model,” *Phys. Rev. B* **93**, 045116 (2016).
- [53] Boris Ponsioen, Sangwoo S. Chung, and Philippe Corboz, “Superconducting stripes in the hole-doped three-band Hubbard model,” *Phys. Rev. B* **108**, 205154 (2023).
- [54] M. Scheb and R. M. Noack, “Finite projected entangled pair states for the Hubbard model,” *Phys. Rev. B* **107**, 165112 (2023).
- [55] Song Cheng, Lei Wang, and Pan Zhang, “Supervised learning with projected entangled pair states,” *Phys. Rev. B* **103**, 125117 (2021).
- [56] Tom Vieijra, Laurens Vanderstraeten, and Frank Verstraete, “Generative modeling with projected entangled-pair states,” *arXiv:2202.08177* (2022).
- [57] Seunghoon Lee, Joonho Lee, Huanchen Zhai, Yu Tong, Alexander M Dalzell, Ashutosh Kumar, Phillip Helms, Johnnie Gray, Zhi-Hao Cui, Wenyan Liu, *et al.*, “Evaluating the evidence for exponential quantum advantage in ground-state quantum chemistry,” *Nature Communications* **14**, 1952 (2023).
- [58] Thomas Barthel, Carlos Pineda, and Jens Eisert, “Contraction of fermionic operator circuits and the simulation of strongly correlated fermions,” *Phys. Rev. A* **80**, 042333 (2009).
- [59] Zheng-Cheng Gu, Frank Verstraete, and Xiao-Gang Wen, “Grassmann tensor network states and its renormalization for strongly correlated fermionic and bosonic states,” *arXiv:1004.2563* (2010).
- [60] Iztok Pižorn and Frank Verstraete, “Fermionic implementation of projected entangled pair states algorithm,” *Phys. Rev. B* **81**, 245110 (2010).
- [61] Zheng-Cheng Gu, “Efficient simulation of Grassmann tensor product states,” *Phys. Rev. B* **88**, 115139 (2013).
- [62] Sukhwinder Singh, Robert N. C. Pfeifer, and Guifre Vidal, “Tensor network states and algorithms in the presence of a

- global U(1) symmetry,” *Phys. Rev. B* **83**, 115125 (2011).
- [63] B. Bauer, P. Corboz, R. Orús, and M. Troyer, “Implementing global abelian symmetries in projected entangled-pair state algorithms,” *Phys. Rev. B* **83**, 125106 (2011).
- [64] A. W. Sandvik and G. Vidal, “Variational quantum Monte Carlo simulations with tensor-network states,” *Phys. Rev. Lett.* **99**, 220602 (2007).
- [65] Norbert Schuch, Michael M. Wolf, Frank Verstraete, and J. Ignacio Cirac, “Simulation of quantum many-body systems with strings of operators and Monte Carlo tensor contractions,” *Phys. Rev. Lett.* **100**, 040501 (2008).
- [66] Ling Wang, Iztok Pižorn, and Frank Verstraete, “Monte Carlo simulation with tensor network states,” *Phys. Rev. B* **83**, 134421 (2011).
- [67] Sebastian Wouters, Brecht Verstichel, Dimitri Van Neck, and Garnet Kin-Lic Chan, “Projector quantum Monte Carlo with matrix product states,” *Phys. Rev. B* **90**, 045104 (2014).
- [68] See Supplemental Material including Refs. [76–78], for Grassmann tensor network representations and additional numerical results.
- [69] Sandro Sorella, “Green function monte carlo with stochastic reconfiguration,” *Phys. Rev. Lett.* **80**, 4558–4561 (1998).
- [70] Eric Neuscamman, C. J. Umrigar, and Garnet Kin-Lic Chan, “Optimizing large parameter sets in variational quantum monte carlo,” *Phys. Rev. B* **85**, 045103 (2012).
- [71] Tom Vieijra, Jutho Haegeman, Frank Verstraete, and Laurens Vanderstraeten, “Direct sampling of projected entangled-pair states,” *Phys. Rev. B* **104**, 235141 (2021).
- [72] Roberto Olivares-Amaya, Weifeng Hu, Naoki Nakatani, Sandeep Sharma, Jun Yang, and Garnet Kin-Lic Chan, “The ab-initio density matrix renormalization group in practice,” *The Journal of Chemical Physics* **142**, 034102 (2015).
- [73] Huanchen Zhai and Garnet Kin-Lic Chan, “Low communication high performance ab initio density matrix renormalization group algorithms,” *The Journal of Chemical Physics* **154**, 224116 (2021).
- [74] Huanchen Zhai, Henrik R. Larsson, Seunghoon Lee, Zhi-Hao Cui, Tianyu Zhu, Chong Sun, Linqing Peng, Ruoqing Peng, Ke Liao, Johannes Tölle, Junjie Yang, Shuoxue Li, and Garnet Kin-Lic Chan, “Block2: A comprehensive open source framework to develop and apply state-of-the-art DMRG algorithms in electronic structure and beyond,” *The Journal of Chemical Physics* **159**, 234801 (2023).
- [75] Huanchen Zhai, Henrik R Larsson, Seunghoon Lee, and Zhi-Hao Cui, “Block2: Efficient mpo implementation of quantum chemistry DMRG. <https://github.com/block-hczhai/block2-preview>,” (2024).
- [76] Quinten Mortier, Lukas Devos, Lander Burgelman, Bram Vanhecke, Nick Bultinck, Frank Verstraete, Jutho Haegeman, and Laurens Vanderstraeten, “Fermionic tensor network methods,” *SciPost Phys.* **18**, 012 (2025).
- [77] Yang Gao, Huanchen Zhai, Johnnie Gray, Ruoqing Peng, Gunhee Park, Wen-Yuan Liu, Eirik F. Kjønsstad, and Garnet Kin-Lic Chan, “Fermionic tensor network contraction for arbitrary geometries,” *arXiv:2410.02215* (2024).
- [78] John W. Negele and Henri Orland, *Quantum Many-Particle Systems* (Westview Press, 1998).